REPORT NO. FRA-ORD&D-74-28

STUDY OF REACTION FORCES IN A SINGLE SIDED LINEAR INDUCTION MOTOR (SLIM)

J.J. Stickler

JANUARY 1974

FINAL REPORT

Prepared for:
DEPARTMENT OF TRANSPORTATION
Federal Railroad Administration
Office of Research, Development, and Demonstrations
Washington DC 20590

Technical Report Documentation Page

1. Report No. FRA-ORD&D-74-28	2. Government Accession No.	3. Recipient's Catalog No.

4. Title and Subtitle STUDY OF REACTION FORCES IN A SINGLE SIDED LINEAR INDUCTION MOTOR (SLIM)	5. Report Date January 1974 6. Performing Organization Code
7. Author(s) J.J. Stickler	8. Performing Organization Report No. DOT-TSC-FRA-73-10
9. Performing Organization Name and Address Department of Transportation Transportation Systems Center Kendall Square Cambridge MA 02142	10. Work Unit No. (TRAIS) RR405/R4308 11. Contract or Grant No.
12. Sponsoring Agency Name and Address Department of Transportation Federal Railroad Administration Office of Research, Development, & Demon. Washington DC 20590	13. Type of Report and Period Covered Final Report July 72 - June 73 14. Sponsoring Agency Code

15. Supplementary Notes

16. Abstract

SLIM reaction forces were measured on a laboratory model having aluminum and aluminum-iron secondaries and the results were correlated with the theoretical forces derived for different idealized SLIM models. The first part of the report discusses wave solutions for single- and multi-region secondaries utilizing the Maxwell Stress Tensor to evaluate the thrust and normal forces. The second part of the report presents data of thrust and normal forces as a function of the stator excitation frequency for different SLIM configurations. The results are helpful both in providing an insight into improved SLIM design and in defining those applications in which the SLIM possesses certain advantages over its double-sided counterpart, as for example, in the application of the LIM to levitated high-speed vehicles.

The correlation of the experimental data with theory is generally fair to good. An exception to the above occurs for the composite SLIM operated at low 'slip frequencies', which gives considerably lower thrust than predicted by theory. Suggestions are made for refining the theory to include boundary and magnetic saturation effects. Further laboratory studies are indicated in those areas where good correlation of experiment with theory is lacking.

17. Key Words Single-Sided Linear Induction Motor, Reaction Forces, Magnetic Diffusion	18. Distribution Statement DOCUMENT IS AVAILABLE TO THE PUBLIC THROUGH THE NATIONAL TECHNICAL INFORMATION SERVICE, SPRINGFIELD, VIRGINIA 22151.

19. Security Classif. (of this report) Unclassified	20. Security Classif. (of this page) Unclassified	21. No. of Pages 84	22. Price

Form DOT F 1700.7 (8-72)

Reproduction of completed page authorized

PREFACE

This report presents the results of reaction force studies made on a practical Single Sided Linear Induction Motor (SLIM). Since the initial Linear Induction Motor (LIM) studies undertaken by Laithwaite & Associates at Imperial College, London, England, other LIM programs have evolved in a number of countries, among them France, Germany, Japan, and the United States. For the most part, these programs have centered around high-speed applications of the double-sided linear induction motor (DLIM). The Tracked Air Cushion Research Vehicle (TRACV) and the Urban Tracked Air Cushion Vehicle (UTACV), under development in the United States by the FRA Office of Research Development and Demonstrations, are examples of such programs. In recent years, the single-sided linear induction motor (SLIM) has been the subject of extensive analytical study by a number of organizations in the United States, including TRW, General Motors, Massachusetts Institute of Technology, General Electric, and University of Kentucky. The latter two organizations have extended the SLIM reaction force studies to high speeds using rotating wheel techniques to simulate practical operating conditions.

The author wishes to express his appreciation to U.S. Steel for supplying numerous iron specimens used in the laboratory tests and to ARMCO Steel for furnishing selected steel samples. Credits are due to Mr. R. Wlodyka for fabricating certain solid-state circuitry used in the reaction force tests and to Mr. L. Devanna for assisting in the measurements during the early phases of the program. The author also wishes to thank Professor J. Melcher for his critical comments and helpful suggestions in the review of this report.

CONTENTS

CONTENTS (CONT'D)

LIST OF ILLUSTRATIONS

LIST OF ILLUSTRATIONS (CONT'D)

LIST OF ILLUSTRATIONS (CONT'D)

LIST OF SYMBOLS

A_1	Magnetomotive force
$\bar{A}$	Magnetic vector potential
$B_x^{(n)}, B_y^{(n)}$	x,y flux density components at n-th interface
b	Thickness of SLIM conducting region
d	Thickness of SLIM ferromagnetic region
$\bar{E}$	Electric field
F_x, F_y	x and y-directed reaction force components
g	Airgap distance
$\bar{J}_1$	Primary current density amplitude
$\bar{K}_1$	Primary surface current density amplitude
k	Wave number in free space
$\bar{\bar{M}}$	Maxwell stress tensor
s	Slip
kw	Winding coefficient of primary winding
$\bar{\bar{T}}$	Generalized transfer matrix
$\bar{\bar{T}}_n$	Transfer matrix associated with n-th layered region
w	Stator width (core height)
x	Coordinate axis in traveling wave direction
y	Coordinate axis normal to primary current sheet
z	Coordinate axis in plane of current sheet and perpendicular to traveling wave direction
α	Complex wave number in conducting region
α_r, α_i	Real and imaginary components of α
Δ_n	Thickness of n-th layered region
δ	Skin depth
η	Effective wave number of SLIM with finite thickness secondary

LIST OF SYMBOLS (CONT'D)

μ_{iron}	Relative permeability of ferromagnetic region
σ	Electrical conductivity
τ_p	Pole pitch equal to half-wavelength of x-directed excitation wave
ω	Angular frequency

1. INTRODUCTION

Considerable interest has evolved in recent years in the use of the Linear Induction Motor (LIM) as the propulsion drive for future high speed trains. The development programs in the field of high speed ground transportation have concentrated on the Double-Sided Linear Induction Motor (DLIM) because of its favorable symmetry for applications requiring only propulsion. The Single-Sided Linear Induction Motor (SLIM), on the other hand, has not been utilized to the same extent as its double-sided counterpart. However, it has recently become apparent that there are important technological problems associated with the use of the DLIM for railway transportation. The most significant problem, that of switching the moving vehicle to alternate railway tracks, is more easily solved through the use of the SLIM. In addition to the advantage of ease of vehicle switching, the SLIM offers the further possibility of vehicle levitation through effective utilization of the normal electromagnetic forces in the SLIM.

The lack of available data on SLIM performance has been a factor which has tended to hinder more rapid development. Without such data it becomes more difficult to anticipate the most suitable SLIM design for a particular application and to estimate its projected performance. One of the objectives of this report is to make available test results obtained from a laboratory study of a SLIM. Data of measured thrust and normal force as a function of slip frequency are summarized for different SLIM configurations and dimensional parameters.

A further objective of this report is the correlation of measured data with theory using the results obtained from the solution of the wave equation for various mathematical SLIM models. Attention is drawn to those areas where additional studies are needed to improve correlation between theory and experiment. An attempt is made to present the data and theoretical results in a form which is amenable to further analytical development.

A review of the literature reveals that very little has been published on the empirical characteristics of the SLIM. Most of the technical publication in this field have dealt with mathematical treatments of idealized SLIM models. Ooi and White (1) have considered the SLIM and developed expressions for simple configurations where the skin effect on the secondary side has been neglected. More recently Lipkis and Wang (2) have treated a SLIM having a multiregion secondary using vector potential solutions of the wave equation. The concept of wave impedance and its application to field solutions of composite secondaries is discussed in the classic paper by Cullen and Barton (3). A number of publications dealing with the double-sided LIM are adaptable for treatment of SLIMs with iron backing. Such publications include the original analysis of edge effects by Russel and Norsworthy (4) and the more recent treatment by Bolten (5,6). The effect of magnetic saturation of the secondary back iron and its effect on SLIM performance has been considered by Dukowitz (7). Yee and Wilson (8) have analyzed saturation effects in solid-rotor induction machines using an equivalent circuit approach, and have compared measured secondary admittance with that predicted by theory. The application of the Maxwell Stress Tensor, upon which many field treatment rely for the evaluation of the SLIM reaction forces, is discussed in textbooks (8) dealing with classical theory of electromagnetism.

The subject material in the report is divided into two parts. The first part summarizes the wave solutions for different SLIM models and uses the Maxwell Stress Tensor to evaluate the traction and normal force components. The second part presents the results of reaction force measurements conducted with different SLIM configurations and analyzes the results in terms of the theory developed in the first part of the report.

Section 2.2 gives a general discussion of SLIM models. Subsection 2.2.1 derives the transfer relations for flux density components in a multiregion SLIM and presents background material required for subsequent mathematical treatments. Section 2.3 and subsections 2.3.1 through 2.3.6 treat solutions for single- and conposite-layered SLIMs. Section 2.4 gives the results of a computer study of flux distribution in a metal-ferromagnetic SLIM secondary. The experimental part of the SLIM program is covered in Section 2.5 and related subsections 2.5.1 through 2.5.6. Conclusions and suggestions for future investigations are outlined in Section 3.0.

2. TECHNICAL DISCUSSION

2.1 THE SLIM: AN ANALYSIS AND EXPERIMENTAL STUDY

An important objective of this program is the correlation of experimental reaction forces of a laboratory SLIM with theoretical reaction forces computed from wave solutions of idealized models. The technical discussion, therefore, begins with review of SLIM models and their wave solutions and later presents empirical reaction force data for purposes of correlation. The SLIM model comprises a traveling current surface wave interacting with multi-region secondaries. The surface wave is assumed to be described by a single frequency and spatial harmonic.

The fictitious current density (amps/m) wave is related to the stator current winding distribution by Fourier analysis. The technique for resolving the stator ampere-turns distribution into an equivalent traveling current density wave is treated in the text by Yamamura (10, p. 15). The amplitude of the primary current density wave, J_1 (amps/m), is related to the equivalent magnitude of a magnetomotive force wave, A_1, (amps), by $J_1 = A_1\pi/\tau_p$, where τ_p is the pole pitch equal to one-half wavelength of the excitation wave. If each coil in a phase winding has N turns and conducts a current of $\sqrt{2}\ I_1$ amperes peak, the combined action of the three-phase currents produces a traveling magnetomotive force given by

$$A_1 = \frac{6\sqrt{2}\ NI_1k_w}{\pi}$$

Here k_w is the winding factor coefficient of the primary winding. The expression for the primary current density amplitude is therefore

$$J_1 = \frac{6\sqrt{2}\ NIk_w}{\tau_p} \qquad (1)$$

The stator used in the SLIM test program is the LIM TECH Model LT15/7/6/110 obtained from LIM TECH Inc. of Santa Monica, California. It has a designed synchronous speed of 22.5 mph at 60 Hz/sec and a capability of developing 100 pounds thrust (for a limited period of time) when operated with a suitable composite aluminum-iron secondary. The relevant stator parameters are listed in the table below.

TABLE 1 SLIM STATOR PARAMETERS

Number of Poles	= 6
Pole Pitch (p)	= 2.25"
Stack Height (w)	= 7"
Turns per Coil (N)	= 37
Coils per Phase	= 3
Number of Slots	= 20
Winding Pitch	= 2/3
Winding Coefficient (k_w)	= .827

Winding pitch in the above table is defined as the ratio of coil span to pole pitch.

2.2 MATHEMATICAL SLIM MODELS

As a preliminary to the discussion of wave solutions for different mathematical SLIM models to be presented in subsequent sections, it is desirable to review the various factors contributing to flux perturbations in SLIMs. These factors are directly related to the finite size of the SLIM and the resulting boundary conditions which are thereby imposed. For purposes of discussion, these boundary conditions can be classified according to which of three directions they take into account. The finite length of the SLIM in the thrust direction (x) brings in end-effects. The finite width in a direction parallel to the rail (secondary) but transverse to the thrust direction (z) brings in boundary conditions representing the edge-effects of the SLIM. The direction transverse to both the rail and the thrust directions or <u>normal direction</u> (y) successively transverses the primary structure, the air-gap, the metal secondary, the ferromagnetic backing if any and the "free-space" region beyond the rail structure. The decay of the magnetic field in this normal direction usually dominates in determining the performance of a practical SLIM. For this reason, it is given primary attention in the mathematical models developed in the following.

The model used in the mathematical treatment of the SLIM consists of parallel layered regions of conducting and ferromagnetic media, bounded at the lower interface by a traveling current density wave. Figure 1 presents a sketch of the model defining the coordinate axes and relevant SLIM parameters. It is assumed that the width and length of the SLIM are sufficiently large that end and edge-effects are negligible. That is, a single spatial harmonic sufficies to describe the y-z dimensional dependence of the fields.

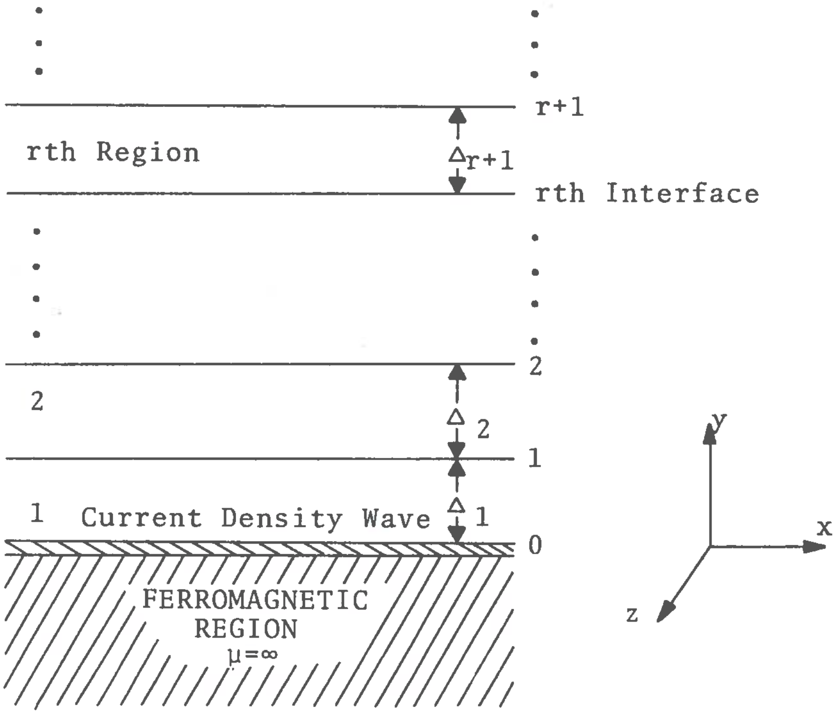

Figure 1. Sketch of Generalized SLIM with Multi-layered Secondary

The currents which flow through the edge windings outside the active region of the stator surface constitute longitudinal currents flowing in the thrust direction. The cross-flux generated by these longitudinal currents lies in a plane perpendicular to the normal flux component and therefore does not couple to the active components of the secondary current.(5) For a composite SLIM with a metal plate-iron backing secondary, this cross-flux (or leakage flux) produces eddy currents in the iron backing region which are not suppressed by iron laminations designed to suppress the transverse secondary currents. The description of the leakage flux in an equivalent circuit analysis, therefore, requires circuit parameters taking into account the anisotropy and this adds an additional degree of complexity to the problem.

The introduction of boundaries limiting the active area of the SLIM, i.e., width and length, complicates the solution of the magnetic diffusion equation. The propagation vector, which defines the direction of wave propagation normal to the em contours of constant phase, is no longer confined to the x-y plane but can now lie along any direction in space. Bolton(5) has shown in the case of the double-sided LIM, which approximates a SLIM with iron backing width equal to that of the stator, the solution of the magnetic diffusion equation leads to two additional waves which travel inwards from the stator edges along the ± z-directions. The interaction of these flux waves with secondary currents flowing in the thrust direction can result in a sidewise (lateral) force of considerable magnitude for certain SLIM configurations(5).

The boundary conditions at the SLIM terminations along the thrust direction causes additional nonuniformities in the surface flux distribution. These flux perturbations take the form of damped sinusoids called entrance and exit end-effect (10,11) waves. At unity slip, both waves are generally highly damped and can usually be neglected; at speeds near synchronous, the entrance end-effect wave can become large and its effect should be included in more exact mathematical treatments.

Magnetic saturation of the iron backing region in the SLIM secondary alters the propagation characteristics of the surface flux waves. In practice, some magnetic saturation of the back iron is possible since efficient use of the SLIM involves its operation near the region of onset of magnetic saturation.(7, p. 2). Localized regions of saturation could exist near the stator edges for SLIMS with large goodness factors(12). The wave solutions required to describe the flux distribution must include both spatial and temporal harmonics, since the magnetic permeability will generally be a function of space and time. The connection between wave harmonics differing by unity in their harmonic orders is provided by the time-varying permeability. The effect of magnetic saturation within a limited depth inside the iron region should be considered in more rigorous SLIM treatments. Because the above considerations increase the complexity of the problem, they are generally omitted in favor of simplier SLIM models which render the solution more tractable.

The following sections treat the exact solutions and their limiting counterparts of idealized SLIM models with multi-region secondaries. Boundary effects (edge effect and end effects), magnetic saturation, and flux leakage effects are neglected in the discussions. The correlation of the theoretical results with empirical data will be examined later in the report.

2.2.1 SLIM Model and Wave Solutions

The SLIM consists basically of a planar structure of electrical windings (stator) capable of generating a traveling surface flux wave which interacts electromechanically with a planar secondary structure. The interaction between the primary stator and secondary reaction rail results from Lorentz forces acting on the moving charges flowing the secondary. The SLIM secondary is assumed to be planar and to be separated from the primary by an equidistant airgap separation distance.

A simplified diagram of a SLIM model illustrating the basic arrangement of primary and secondary is shown in Figure 1. In the

SLIM model, the stator is replaced by a semi-infinite slab of infinite permeability which supports a current density wave traveling along the surface of the slab in the x-direction. Above the current density wave lies a multi-region secondary, the thickness of the n-th region being equal to Δ_n. The model assumes the primary and secondary to be sufficiently wide in the z-direction and long in the x-direction (direction of primary current wave) that edge effects and end effects can be neglected. The primary current wave has a time (t) and x-dependency constrained by the relationship $\exp(j\omega t - kx)$ where $\omega = 2\pi f$ is the angular frequency of current excitation, $k = \pi/\tau_p$ is the wave number in the x-direction.

The development of the mathematical SLIM model in this section follows the approach of Lipkis and Wang(2). It consists of applying the magneto-quasi-static approximation to Maxwell's electromagnetic equations using the idealized model shown in Figure 1. The linear induction motor is treated as a boundary value problem in which the Laplacian magnetic fields in the airgap must match the traveling current wave at the stator surface. Once the magnetic fields are solved, the thrust and normal forces can be evaluated either by use of the Maxwell Stress Tensor or by the J x B method plus a separate magnetization force calculation.

The magneti-quasi-static equations, applicable to regions of constant permeability are:

$$\nabla \times \overline{B} = \mu \overline{J} \qquad (2)$$

$$\nabla \times \overline{E} = -d\overline{B}/dt \qquad (3)$$

$$\nabla \cdot \overline{B} = 0$$

$$\overline{J} = \sigma(\overline{E} + \overline{V} \times \overline{B}) \qquad (4)$$

In the above equations B is the magnetic flux density, μ the permeability, J the electric current density, E the electric field intensity, σ the electric conductivity, V the velocity of the moving medium, and H the magnetic field intensity. The displacement current, $\alpha D/\alpha t$, which is negligible in the frequency range applicable to this study, is omitted in the above equations. Rationalized MKS units are used.

Introducing a vector potential $\overline{A}$, defined such that Equation (4) is automatically satisfied,

$$\nabla x \overline{A} = \overline{B} \tag{5}$$

Substituting the above into Equations (2), (3), and (4) results, after simplification, in

$$\nabla^2 \cdot \overline{A} = \mu\sigma \left[\frac{d\overline{A}}{dt} - \overline{V} \text{ x } (\nabla \text{ x } \overline{A}) \right] \tag{6}$$

where to completely specify $\overline{A}$, $\nabla \cdot \overline{A} = 0$.

Equation (6) reduces to

$$\nabla^2 \cdot \overline{A} = 0$$

when $\sigma = o$ in the air gap and in completely laminated iron regions.

With the assumptions specified previously, the vector potential can be taken as having a component only in the z-direction ($A_x = A_y = 0$ and $A_z = A$).

$$A_z = \left(Ce^{\alpha y} + De^{-\alpha y} \right) e^{\,j(\omega t - kx)} \tag{7}$$

Once the constants C and D are found for each region satisfying the boundary conditions at their respective interfaces, Equations (5-7) can be used to determine the flux density valid within each region.

The propagation number, α, is determined by substituting Equation (7) into Equation (6).

$$\alpha = k \sqrt{1 + j\ R_m} \tag{8}$$

where R_m is the magnetic Reynolds number (2, p. 44) defined as

$$R_m = \frac{\sigma s \omega \mu_o}{k^2}$$

Here s is the slip given by

$$s = \frac{V_s - V}{V_s}$$

where V_s is the phase velocity in the x-direction of the traveling-wave current excitation on the stator.

It is convenient to express the propagation wave number, α, in the form

$$\alpha = \alpha_r + j\alpha_i \ . \qquad (9)$$

In the limit of low excitation frequency,

$$\alpha_r \cong k$$

$$\alpha_i \cong \frac{1}{\delta^2 k}$$

and in the limit of high excitation frequency,

$$\alpha_r \cong 1/\delta$$

$$\alpha_i \cong 1/\delta$$

where δ is the skin depth in the region given by

$$\delta = \sqrt{\frac{2}{\mu\sigma s\omega}} \ . \qquad (10)$$

2.2.1.1 Boundary Conditions and Transfer Matrices - The number of arbitrary constants, C and D, describing the flux density in the secondary is equal to twice the number of regions comprising the secondary. For a N-region secondary, the 2N relations needed to evaluate the constants are determined from the following boundary conditions: (1) The flux density must approach as zero at large y-distance normal to the stator surface. (2) The tangential component of magnetomotive force, H_x, at the stator surface is equal to the effective current density at the stator surface. (3) The normal component of magnetic induction, B_y, is continuous at the N-1 interfaces (not including the stator-air interface) (4). The tangential component of magnetomotive force, Hx is continuous at the N-1 interfaces.

The normal flux density, B_y, and tangential magnetization, H_x, found by substituting Equation (7) in Equation (5) are

$$B_y = \frac{-\alpha A}{\alpha x} = jk\left(Ce^{\alpha y} + De^{-\alpha y}\right)$$

$$H_x = \frac{1}{\mu}\,\frac{\alpha A}{\alpha y} = \frac{\alpha}{\mu}\left(Ce^{\alpha y} - De^{-\alpha y}\right)$$

where C, D are arbitrary constants and α is the propagation number associated with the specified region. Eliminating the constants, C, D in the above equations leads to the transfer relation describing the $B_y^{(n)}$, $H_x^{(n)}$ components at the n-th interface in terms of the corresponding components at the n+1th interface (13),

$$\begin{bmatrix} B_y^{(n)} \\ H_x^{(n)} \end{bmatrix} = \begin{bmatrix} \cosh\alpha_{n+1}\Delta_{n+1} & \dfrac{-j\mu_{n+1}k}{\alpha_{n+1}} \sinh\alpha_{n+1}\Delta_{n+1} \\ \dfrac{-\alpha_{n+1}}{j\mu_{n+1}k} \sinh\alpha_{n+1}\Delta_{n+1} & \cosh\alpha_{n+1}\Delta_{n+1} \end{bmatrix} \cdot \begin{bmatrix} B_y^{(n+1)} \\ H_x^{(n+1)} \end{bmatrix} \tag{11}$$

or

$$\begin{bmatrix} B_y^{(n)} \\ H_x^{(n)} \end{bmatrix} = \overline{\overline{T}}_{n+1} \cdot \begin{bmatrix} B_y^{(n+1)} \\ H_x^{(n+1)} \end{bmatrix} \tag{12}$$

where T_{n+1} is the transfer matrix defined by Equation (11) for the region of layer thickness Δ_{n+1}. In a generalized layered structure comprising r layers, the transfer relation takes the form,

$$\begin{bmatrix} B_y^{(n)} \\ \\ H_x^{(n)} \end{bmatrix} = \overline{\overline{T}}_{n+1} \cdot \overline{\overline{T}}_{n+2} \cdot \overline{\overline{T}}_{n+3} \cdot \cdot \cdot \overline{\overline{T}}_{n+r} \cdot \begin{bmatrix} B_y^{(n+r)} \\ \\ H_x^{(n+r)} \end{bmatrix} \tag{13}$$

If the nth interface is taken to be the surface of the primary current wave, i.e., n = 0, the continuity of H_x requires (14)

$$H_x^{(o)} = -K_1$$

if the permeability of the region below the primary current sheet is assumed to be effectively infinite. At the rth interface corresponding to the most distant interface from the primary current sheet (neglecting the interface at infinity), boundary condition (1) takes the form

$$H_x^{(r)} = -\frac{\alpha_r B_y^{(r)}}{j\mu_r k} \tag{15}$$

as found by taking the limit $\Delta_r \to \infty$ of Equation (11) and assuming $\mathrm{Re}(\alpha_r) > 0$. Equations (13) through (15) are sufficient to determine the field (and force) components associated with an arbitrary multilayered secondary structure once the transfer matrices, $\overline{\overline{T}}$, have been specified.

2.2.1.2 <u>Maxwell Stress Tensor</u> - For the two-dimensional magnetic field considered in this study, the Maxwell stress tensor, $\overline{\overline{M}}$, may be written as

$$\overline{\overline{M}} = \frac{1}{\mu} \begin{bmatrix} \frac{1}{2}\left(B_x^2 - B_y^2\right) & B_x B_y & 0 \\ \\ B_y B_x & \frac{1}{2}\left(B_y^2 - B_x^2\right) & 0 \\ \\ 0 & 0 & -\frac{1}{2}\left(B_x^2 + B_y^2\right) \end{bmatrix} \tag{16}$$

The force acting in the m-direction is

$$F_m = \oint M(mn)\ n_n dA \tag{17}$$

where n_n is the unit normal vector in the direction specified by its subscript. It is usual to integrate Equation (17) over an area of stator surface equal to the width of the stator and one wavelength along the longitudinal axis of the stator. The remaining surface areas required to complete the surface integration can be shown to contribute nothing to the average force.

The substitution of the tensor components M(mn) in Equation (16) gives for the time average force components

$$F_x = \frac{1}{2} \iint \text{Real}\left(\hat{H}_x \hat{B}_y^*\right) dxdz \tag{18}$$

$$F_y = \frac{1}{4} \iint \text{Real}\left(\frac{\hat{B}_y \hat{B}_y^*}{\mu_o} - \mu_o \hat{H}_x \hat{H}_x^*\right) dxdz \tag{19}$$

where $\hat{B}_y$ and $\hat{B}_x$ are the complex amplitudes defined by the general form $\overline{B}$ = Re $\hat{B}$ exp(jωt-kx) evaluated in the airgap where $\mu = \mu_o$. For example; evaluated at the stator interface, $\hat{B}_x = B_x(y = o)$. Since the forces given by Equations (18) and (19) must be independent of the position within the airgap at which B_x, B_y are defined, the above integrations must yield the same forces irrespective of whether the integration is carried out over the stator surface or a corresponding area at the air-aluminum interface.

2.3 WAVE SOLUTIONS OF SPECIFIC SLIM MODELS

The wave solutions for different SLIM models will now be examined using the mathematical techniques developed in the previous section. The first SLIM models examined metal-only secondaries while later SLIM models treat the more general case of composite metal-ferromagnetic secondaries. In each case, it is assumed that electrical conductivity and magnetic permeability are isotropic, current excitation is of single frequency, and nonlinear phenomena are absent.

2.3.1 SLIM: Finite Thickness Secondary (Air-Metal-Air)

The field solution and force components will now be evaluated for the case of a conducting sheet secondary of finite thickness and separated from the primary current density surface wave by a distance g. Current flow in both primary and secondary is assumed to be in the z-direction and edge current flow along the x-direction is neglected. The latter condition results from the assumption that the primary and secondary extend to infinity in the z-direction.

The wave solution for a SLIM having a single conducting secondary at a fixed distance from a planar current excitation wave reduces to the wave solution of a tri-region secondary having a conducting layered region sandwiched between two parallel layers of air. In the terminology set forth in the previous section, Region 1 corresponds to the air region separating the exciting current sheet and secondary conducting layer, Region 2 is the secondary conductor, and Region 3 is the free space region extending to infinity. Figure 2a shows a sketch of the model with defining parameters. Superscripts designate the interfaces associated with the magnetic field quantities at the layer boundaries.

The transfer matrices, $\overline{\overline{T}}_o$, $\overline{\overline{T}}_1$ relating the field quantities at the n = 0th interface to the corresponding field quantities at the n = 1th interface follow directly from Equation (11) with $n = 0$, $r = 2$, $\alpha_1 = k$, $\alpha_2 = \alpha$, $\alpha_3 = k$, $\Delta_1 = g$, $\Delta 2 = b$. Including the condition that $H_x = -K_1$; multiplication of $\overline{\overline{T}}_o \times \overline{\overline{T}}_1$ gives

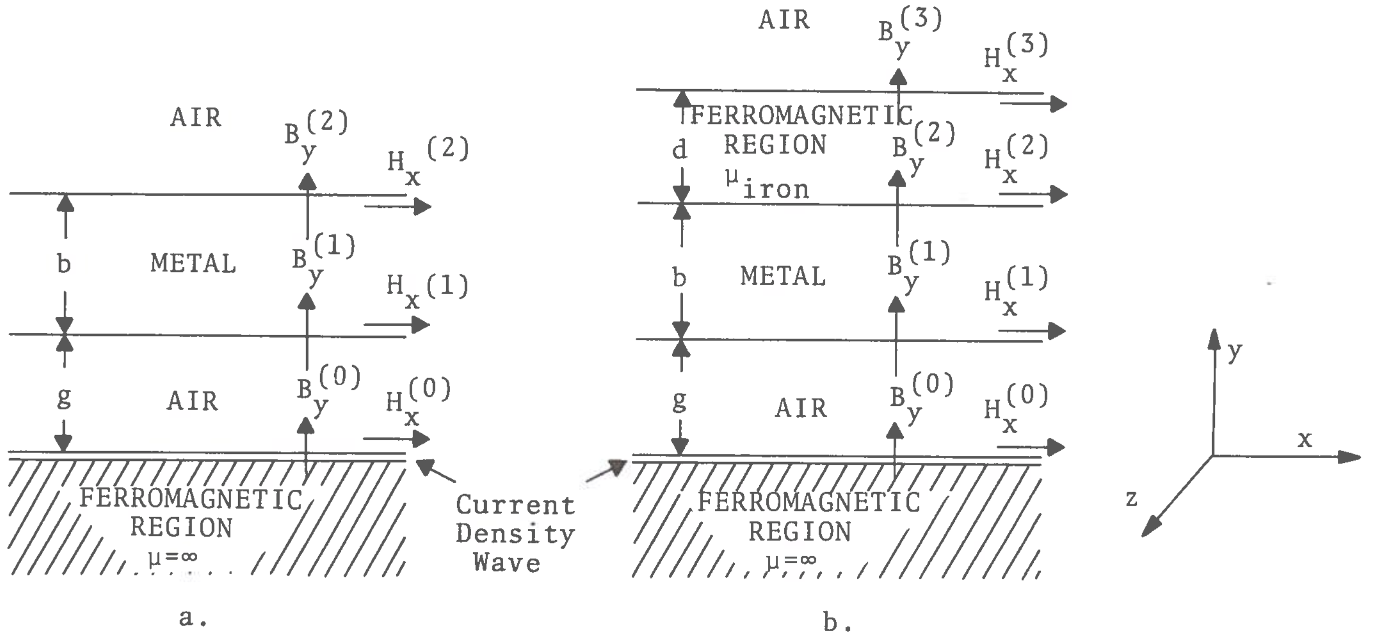

Figure 2. Sketch of Idealized SLIM Models for Metal and Metal-Ferromagnetic Secondaries

$$\begin{bmatrix} B_y^{(o)} \\ \\ -K_1 \end{bmatrix} = \begin{bmatrix} \left(\cosh kg \cosh\alpha b + \frac{\alpha}{k}\sinh kg \sinh\alpha b\right) & \left(\frac{-j\mu_o}{\alpha}k\sinh\alpha b \cosh kg - j\mu_o\sinh kg\cosh\alpha b\right) \\ \left(\frac{1}{j\mu_o}\sinh kg \cosh\alpha b - \frac{\alpha}{j\mu_o k}\cosh kg\sinh\alpha b\right) & \left(\frac{k}{\alpha}\sinh kg\sinh\alpha b + \cosh kg \cosh\alpha b\right) \end{bmatrix} \begin{bmatrix} B_y^{(2)} \\ \\ H_x^{(2)} \end{bmatrix} \tag{20}$$

Since $H_x{}^{(2)} = \frac{jB_y{}^{(2)}}{\mu_o}$, it follows from Equation (20) that

$$B_y{}^{(0)} = j\mu_o K_1 \frac{(\cosh kg + \eta \sinh kg)}{(\sinh kg + \eta \cosh kg)} \tag{21}$$

where

$$\eta = \frac{\cosh\alpha b + \frac{\alpha}{k}\sinh\alpha b}{\cosh\alpha b + \frac{k}{\alpha}\sinh\alpha b} \tag{22}$$

The thrust and normal forces per wavelength, $(2\tau_p)$, follow by using Equations (20) and (21) to evaluate Equations (18) and (19).

$$F_x = 2w\tau_p \, \frac{1}{2}\text{Re}\left(-K_1^* \times B_y^{(o)}\right) = \frac{w\tau_p\mu_o K_1{}^2 \eta_i}{|\eta|^2 \left|\cosh kg + \frac{1}{\eta}\sinh kg\right|^2} \tag{23}$$

$$F_y = 2w\tau_p \, \frac{1}{4}\text{Re}\left[\frac{B_y^{(o)} B_y^{(o)*}}{\mu} - \mu K_1 K_1{}^*\right]$$

$$= \frac{-w\tau_p\mu_o|K_1|^2}{2}\left(\frac{1}{|\eta|^2} - 1\right)\frac{1}{\left|\cosh kg + \frac{1}{\eta}\sinh kg\right|^2} \tag{24}$$

It is desirable at this point to examine the functional dependence of F_x and F_y on η using as independent parameters the angular frequency, ω, and the thickness of the secondary conducting sheet. The thrust and normal forces given by Equations (23) and (24) respectively were computed for values of thickness of secondary conducting layer equal to 3, 6, and 31 mm. For all calculations, the airgap distance was taken as 1 mm and the electrical conductivity of the secondary equal to 2.5×10^7 mhos/meter (for aluminum alloy 6061-T6). The current density amplitude, computed from Equation (1) for the stator phase current of 14 amperes and the motor parameters given in Table 1, was 0.64×10^5 amps/m.

Figures 3 and 4 present the results of the calculations of thrust and normal forces as shown by the solid curves. The thrust becomes maximum at a given current excitation frequency while the normal force increases monotonically with frequency, approaching asymptotically a limiting normal force at high frequencies. The magnitude of the normal force at the frequency corresponding to maximum thrust is about one-half its limiting value at high frequencies.

The dimensional dependence of the thrust and normal forces on secondary thickness is related to the ratio of skin depth to secondary thickness for the SLIM. For the conductivity assumed in the calculations $\left(\sigma_{AL} = 2.5 \times 10^7 \text{mhos/m}\right)$, the computed skin depth is 18.3 mm at the frequency for peak thrust in an infinitely thick secondary, namely 30 Hz/sec. For secondary thicknesses substantially larger than the skin depth, the thrust and normal forces are almost independent of secondary thickness. The 3 and 6 mm thick secondaries illustrate SLIMs having secondary thicknesses less than the skin depth over most of the range of current excitation frequencies.

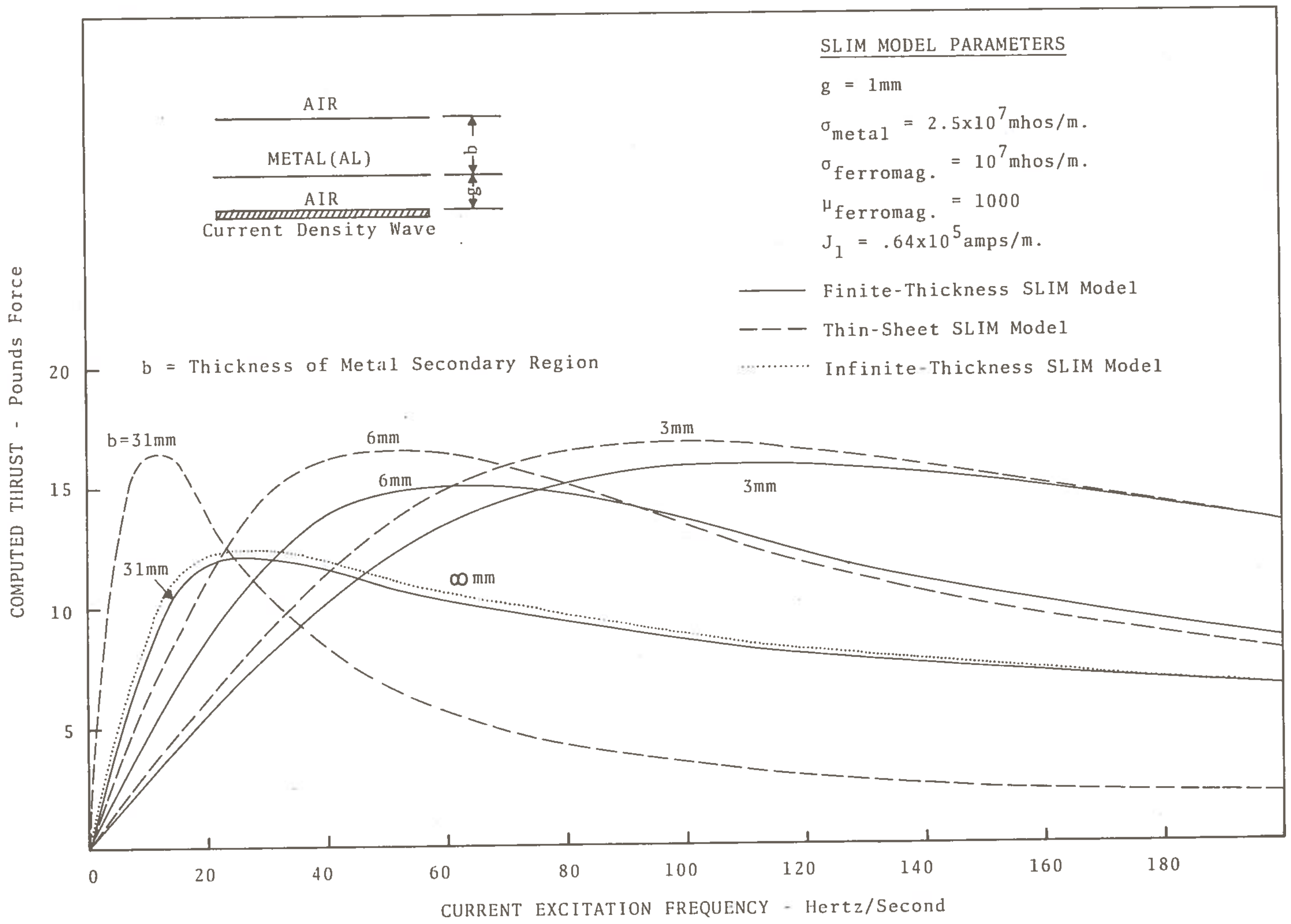

Figure 3. Computed Thrust as a Function of Current Excitation Frequency for SLIM with Aluminum Secondary. Computed Curves Illustrate Finite Thickness, Infinite Thickness, and Thin-Sheet Mathematical SLIM Models

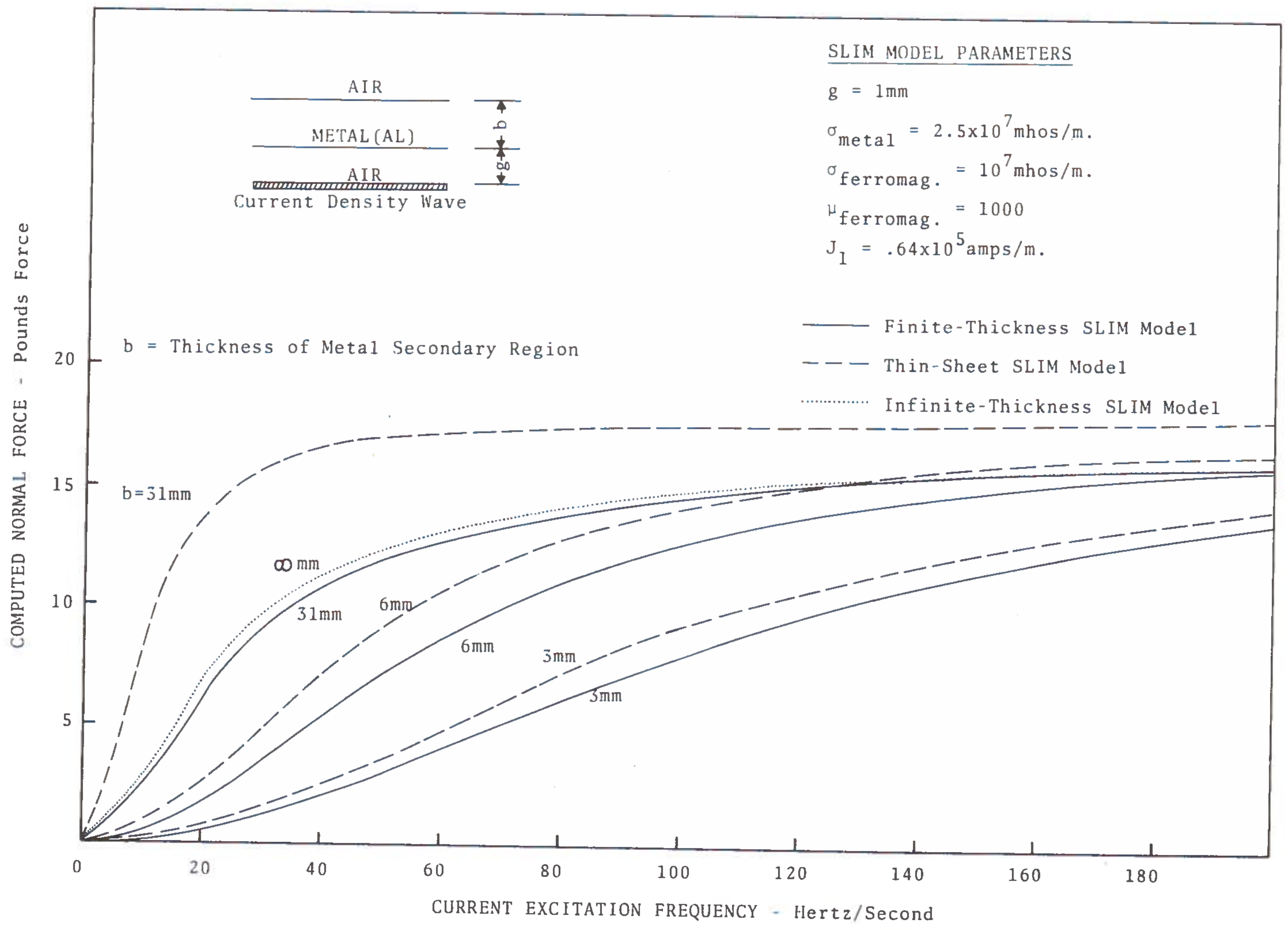

Figure 4. Computed Normal Force as a Function of Current Excitation Frequency for SLIM with Aluminum Secondary. Computed Curves Illustrate Finite Thickness, Infinite Thickness, and Thin-Sheet Mathematical SLIM Models

2.3.2 SLIM: Finite Thickness Secondary: Thin-Sheet Approximation

The solution for the SLIM model in the limiting case of the thin-sheet approximation will now be considered. The solution differs from that of the previous analysis for the finite thickness SLIM model by the restriction that the sheet thickness be now much less than the wavelength of the primary current density wave.

$$kb \ll 1$$

Implicit in the thin sheet approximation is the additional requirement that the sheet thickness be also much less than the skin depth, of the penetrating electromagnetic wave,

$$b \ll \delta$$

The above restrictions can be combined in the single condition involving the propagation number, α, of the wave in the metal.

$$\left|\alpha b\right| = \left|\sqrt{(kb)^2 + j^2\left(\frac{b}{\delta}\right)^2}\right| \ll 1$$

Both primary and secondary currents are assumed to flow in the z-direction. The width of the SLIM in the z-direction is taken to be infinite which eliminates the functional dependence of current and field components on the z-axis coordinate.

The introduction of the above limiting conditions into the expression for η given by Equation (22) results in

$$\eta \to 1 + j\frac{\omega\mu_o\sigma_s}{k} \qquad (25)$$

where ω is now taken to be the 'slip frequency', i.e., $\omega=\omega.s$ and σ_s is the surface conductivity defined as $\sigma_s = b\sigma$. Substitution of the approximate expression for η in Equations (23) and (24) yields for the force components in the thin-sheet approximation,

$$F_x = \frac{\mu_o K_1^{\ 2} \left(\sigma_s \mu_o \omega / k\right) w \tau_p}{\sinh^2 kg \left[\left(1 + \coth\ kg\right)^2 + \left(\frac{\sigma_s \mu_o \omega}{k}\right)^2 \coth^2 kg\right]} \tag{26}$$

$$F_y = \frac{1}{2}\ \frac{\mu_o K_1^{\ 2} \left(\sigma_s \mu_o \omega / k\right)^2\ w \tau_p}{\sinh^2 kg \left[(1 + \coth kg)^2 + \left(\frac{\sigma_s \mu_o \omega}{k}\right)^2 \coth^2 kg\right]} \tag{27}$$

The thrust and normal forces given by Equations (25) and (26) were computed as a function of frequency for the values of sheet thickness, b = 3, 6, and 31 mm. The dashed curves in Figures 3 and 4 give the results of computations for F_x and F_y. For comparison, the stress tensor components computed for the finite sheet thickness case using Equations (23) and (24), are shown by the solid curves.

The maximum thrust in the x-direction occurs at the angular frequency (at unity slip),

$$\omega_{max} = \frac{k}{\sigma b \mu_o} (1 + \tanh\ kg) \tag{28}$$

Thus, the frequency of peak x-directed thrust varies inversely with plate thickness and linearly with airgap distance for small gap separations.

The magnitudes of the force components at the angular frequency ω_{max} are given by

$$F_x = \frac{\mu_o K_1^{\ 2} w \tau_p}{2 \cosh^2 kg (\tanh kg + 1)}$$

$$F_y = \frac{\mu_o K_1^{\ 2} w \tau_p}{4 \cosh^2 kg}$$

2.3.3 SLIM: Infinite Thickness Approximation

The SLIM characteristics for a model based on an infinitely thick secondary conductor positioned at a constant airgap distance from the primary current density wave will now be examined. This model describes the limiting case of a single region secondary (conductor) whose thickness is large compared with both the skin depth, δ, and the wavelength, $2\tau_p$, of the primary current excitation wave.

$$|b\alpha| = \sqrt{(kb)^2 + j2(b/\delta)^2} >> 1$$

Since skin depth varies inversely with frequency, the approximation becomes increasingly better in the limit of high excitation frequencies.

If the above condition is applied to Equation (22) the expression for η takes the form

$$\eta \to \alpha/k$$

The thrust and normal components of force, given by Equations (18) and (19) respectively, reduce in this limit to

$$F_x = \frac{w\tau_p \mu_o K_1{}^2 \alpha_i}{|\alpha|^2 \left|\cosh kg + \frac{k}{\alpha}\sinh kg\right|^2} \tag{29}$$

$$F_y = -\frac{w\tau_p}{2}\mu_o K_1{}^2\left(\frac{k^2}{|\alpha|^2} - 1\right)\frac{1}{\left|\cosh kg + \frac{k}{\alpha}\sinh kg\right|^2} \tag{30}$$

where α_i is the imaginary part of α as defined by Equation (9). The magnitude of the above force components computed as a function of frequency are shown in Figures 3 and 4 by the dotted curves. Comparing these curves with those computed on the basis of the finite thickness SLIM model, it is seen that the agreement is good for a secondary thickness of 31 mm but poor for the secondary thicknesses of 3 and 6 mm.

The angular frequency for maximum thrust in the limit of a vanishingly small airgap (kg<<1) is given by

$$\omega_{max} = \frac{\sqrt{3}\ k^2}{\mu_o \sigma} \tag{31}$$

The thrust and normal forces at the angular frequency of maximum thrust are given in the limit of vanishingly small airgap (kg<<1) by,

$$F_{x_{\text{thin-sheet approximation}}} = \frac{w\tau_p \mu_o K_1^{\,2}}{2\sqrt{2}}$$

$$F_{y_{\text{thin-sheet approximation}}} = \frac{w\tau_p \mu_o K_1^{\,2}}{4\sqrt{2}} \quad .$$

2.3.4 Composite SLIM: (Air-Metal-Ferromagnet-Air) Ferromagnetic Backing of Finite Thickness

The field solution for a SLIM having a composite secondary comprising a conducting plate with iron backing of finite thickness will now be examined. The secondary is assumed to be separated from the exciting primary current wave by a fixed airgap distance g. The ferromagnetic (iron) region is assumed to be laminated in the z-direction so that current flow along the lateral direction is suppressed. A sketch illustrating the SLIM model with defining parameters is shown in Figure 2b.

The electromagnetic problem reduces to one of determining the field solution in a three-region media of air, metal, and ferromagnet with the exciting current density wave located at the position of the first boundary interface. Once the field components (B_y, B_x) in the airgap have been found, the thrust and normal forces can be computed from Equations (18 and 19).

The field components at the current density wave-air interface (n=0) are related to the components at the ferromagnet-air interface (n=3) according to Equation (13). Thus

$$\begin{bmatrix} B_y^{(o)} \\ H_x^{(o)} \end{bmatrix} = \overline{\overline{T}}_o \cdot \overline{\overline{T}}_1 \cdot \overline{\overline{T}}_2 \begin{bmatrix} B_y^{(3)} \\ H_x^{(3)} \end{bmatrix} \tag{32}$$

where $\overline{\overline{T}}_o \cdot \overline{\overline{T}}_1$ is the matrix product as given by the RHS of Equation (20). The transfer matrix, T_2, follows from Equation (11) with n=2, 3=d.

$$\overline{\overline{T}}_2 = \begin{bmatrix} \cosh\alpha_3 d & \dfrac{-j\mu_3 k}{\alpha_3}\sinh\alpha_3 d \\ \dfrac{-\alpha_3}{j\mu_3 k}\sinh\alpha_3 d & \cosh\alpha_3 d \end{bmatrix} \tag{33}$$

Performing the matrix multiplication $\overline{\overline{T}}_o \cdot \overline{\overline{T}}_1 \cdot \overline{\overline{T}}_2$ and introducing the conditions that $H_x^{(o)} = -K_1$ and $H_x^{(3)} = jB_y^{(3)}$ into Equation (32) leads to the expression for the normal flux density component at the current density interface,

$$B_y^{(o)} = j\mu_o K_1 \frac{\cosh kg + \eta' \sinh kg}{\sinh kg + \eta' \cosh kg} \tag{34}$$

where

$$\eta' = \frac{\cosh\alpha_2 b + \xi \sinh\alpha_2 b}{\cosh\alpha_2 b + \frac{1}{\xi}\sinh\alpha_2 b} \tag{35}$$

and

$$\xi = \alpha_2 \frac{1 + \frac{\mu_3}{\mu_o \alpha_3} \tanh\alpha_3 d}{1 + \frac{\alpha_3 \mu_o}{\mu_3} \tanh\alpha_3 d} \tag{36}$$

The subscripts, 2,3, refer to the metal and ferromagnet regions respectively as illustrated in Figure 2b. Substituting Equations (14 and 34) in Equations (18 and 19) gives the desired expressions for thrust and normal forces for a composite SLIM with ferromagnetic backing.

The thrust and normal forces were computed as a function of current excitation frequency for a SLIM having a secondary (aluminum plate) thickness, b=3mm, and ferromagnetic (iron) backing thicknesses, d=0.1, 3.0, and 31 mm. The electrical conductivities of aluminum and iron were taken as 2.5 x 10^7 mhos and 10^7 mhos/m respectively. The current density amplitude was assumed to be 0.46 x 10^5 amps/m. The computed thrust and normal forces are shown by the solid curves in Figures 5 and 6 respectively.

A comparative study of the thrust characteristics given in Figure 5 with those given in Figure 3 shows several interesting points. First, the peak thrust is increased in magnitude by the use of ferromagnetic backing. For the example of the 3 mm aluminum secondary thickness, the peak thrust is increased by a factor of three by the addition of a 0.5 mm thick ferromagnetic backing. Second, the frequency associated with peak thrust is reduced with ferromagnetic backing. For the above example, the backing causes the frequency of peak thrust to decrease from 110 to 35 Hz/sec. Third, the thrust characteristic is relatively independent of backing thickness for backing thicknesses exceeding 0.5 mm.

2.3.5 Composite SLIM: (Air-Metal-Ferromagnet) Thin-Sheet Approximation

The thrust and normal forces will now be examined for a SLIM model comprising a metal-ferromagnetic (backing) secondary in the

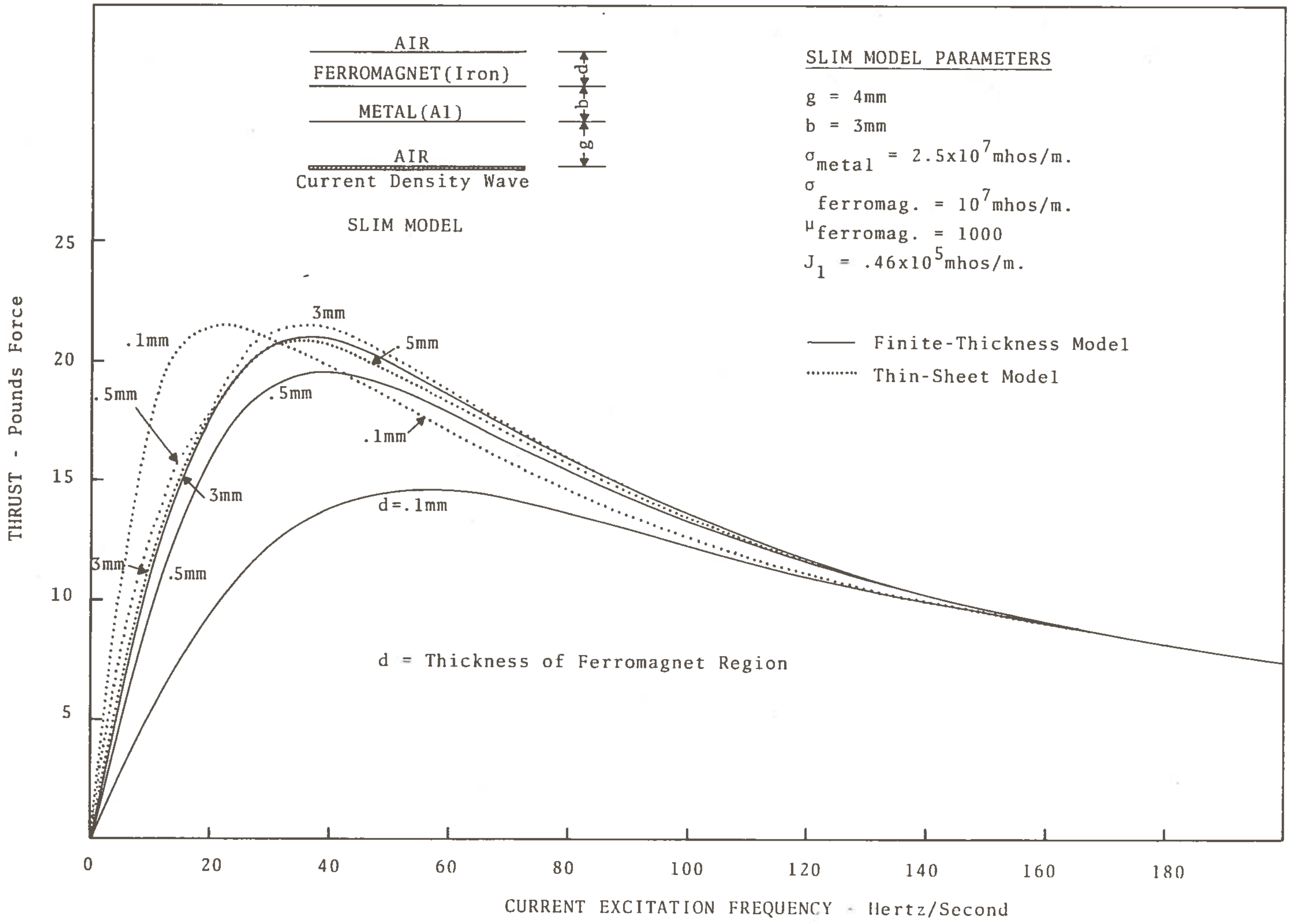

Figure 5. Computed Thrust as a Function of Current Excitation Frequency for SLIM with Composite Aluminum-Iron Secondary. Curves Give Computed Thrust for Finite Thickness Aluminum Secondary and Limiting Case of Thin-Sheet Aluminum Secondary

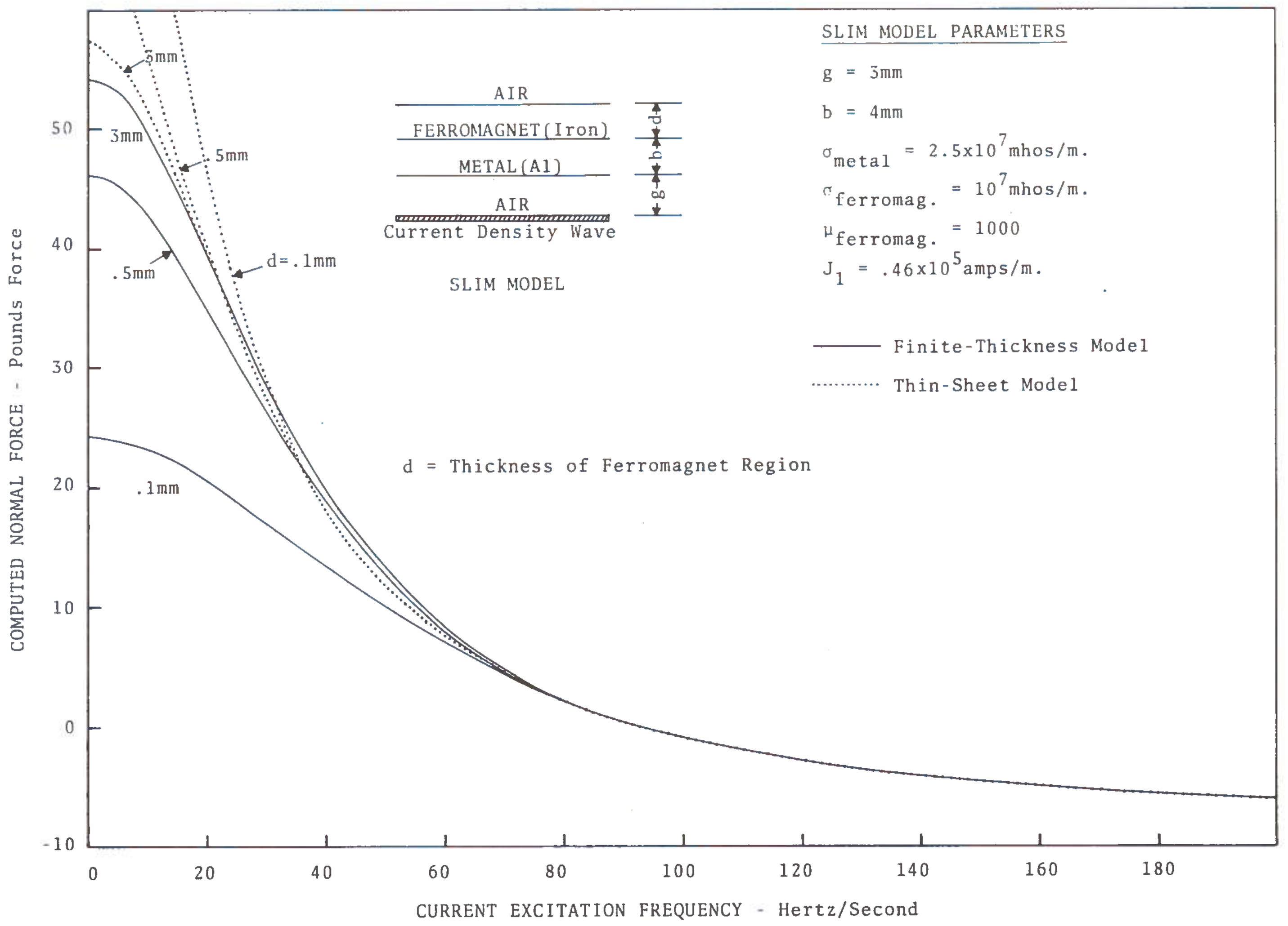

Figure 6. Computed Normal Force as a Function of Current Excitation Frequency for SLIM with Composite Aluminum-Iron Secondary. Curves give Computed Normal Force Thrust for Finite Thickness Aluminum Secondary and Limiting Case of Thin-Sheet Aluminum Secondary

limit of thin secondary metal thickness. The condition applicable to the thin-sheet approximation restricts the metal secondary thickness according to

$$b \ll \frac{1}{|\alpha_2|} \tag{37}$$

The introduction of the above limit into Equation (35) gives

$$\eta' = \frac{1 + \alpha_2 b \xi}{1 + \dfrac{\alpha_2 b}{\xi}}$$

where ξ is defined by Equation (35). Further, if use is made of the condition, $\xi \gg 1$, which is applicable to most practical SLIMs, the above relation reduces to $\eta' \rightarrow 1 + \alpha_2 b \xi$. Since the permeability of ferromagnetic iron is three orders of magnitude larger than that of free space, it is reasonable to approximate ξ by $\xi \rightarrow \frac{\alpha_2 \mu_3}{\alpha_3 \mu_o} \tanh \alpha_3 d$ and η' by

$$\eta' = 1 + \left[kb + j\omega s \mu_o \sigma_s\right] \frac{\mu_3}{\mu_o} \frac{k}{\alpha_3} \tanh \alpha_3 d \tag{38}$$

Combining Equations (38, 34 and 14) with Equations (18, and 19) leads to the following expressions for the thrust and normal forces in a composite SLIM.

$$F_x = w\tau_p \frac{\mu_o K_1^2 \left(\sigma_s \mu_o \omega / k\right)}{\sinh^2 kg \left[(1 + kb \coth kg)^2 + (\sigma_s \mu_o \omega / k)^2 \coth^2 kg\right]} \tag{39}$$

$$F_y = -\frac{w\tau_p \mu_o K_1^2 \left[1 - (kb)^2 - \left(\sigma_s \mu_o \omega / k\right)^2\right]}{2 \sinh^2 kg \left[(1 + kb \coth kg)^2 + \left(\sigma_s \mu_o \omega / k\right)^2 \coth^2 kg\right]} \tag{40}$$

Here the assumption $\frac{\mu_3}{\mu_o}\frac{k}{\alpha_3}kb>>1$ has been used to simplify the form of the above equations and slip, s, has been taken to be unity.

The thrust and normal forces in the thin-sheet approximation were computed from the above relations for examples of composite SLIMs comprising a 3 mm thick aluminum conducting plate with 0.1, 0.5, and 3 mm thick ferromagnetic (iron) backing. The airgap separation distance was taken as 4 mm and the amplitude of the excitation current wave as $.46 \times 10^5$ amps/m. The computed thrust and normal forces are given by the dotted curves shown in Figures 5 and 6.

The figures show that for the SLIM examples chosen, the thin-sheet approximation gives results which are in reasonable agreement with the exact-finite-thickness model for excitation frequencies above 30 Hz/sec. and ferromagnetic backing thicknesses of 0.5 mm and greater. The agreement is considerably better if the 0.1 mm thick backing example is discarded as being much too thin for practical applications. The thin-sheet approximation then agrees well with the finite thickness model for thrusts computed over all frequencies (0-200 Hz/sec) and normal forces computed above 20 Hz/sec.

The angular frequency of peak thrust determined from Equation (40) in the limit of small airgap (kg<<1) is

$$\omega_{max} \approx \frac{k^2}{\sigma\mu_o}(1 + g/b). \tag{41}$$

The corresponding thrust and normal forces at this angular frequency are

$$F_{x_{max}} \approx \frac{w\tau_p\mu_o K_1{}^2}{2kb}$$

$$F_{y_{max}} \approx \frac{w\tau_p\mu_o K_1{}^2}{4(kb)^2} \quad .$$

2.3.6 Composite SLIM: (Air-Metal-Ferromagnet-Air) Zero-Versus-Nonzero Electrical Conductivity of Ferromagnetic Backing

The effect of ferromagnetic conductivity on the SLIM reaction force characteristics is now examined. The SLIM model is identical to that studied in the previous section, i.e., secondary of aluminum with iron backing, except that the conductivity of the ferromagnetic (iron) backing is assigned values of zero and the nominal conductivity of iron.

The propagation constant in the ferromagnetic region is given by

$$\alpha_{iron} = \sqrt{k^2 + j\mu_{iron}\,\sigma_{iron}\omega s}$$

The assumption of zero ferromagnetic conductivity leads to a real propagation constant $\alpha_{iron} = k$, while nonzero ferromagnetic conductivity results in a complex propagation constant which at nonzero frequency can be approximated by $\alpha_{iron} \simeq \frac{1}{\delta_{iron}}(1 + j)$ where δ_{iron} is the skin depth in the ferromagnetic region defined by Equation (10). Since the condition implied in the latter equation requires $1/\delta_{iron} >> k$, the diffusion of magnetic flux in the nonzero ferromagnetic conductivity region will be characterized by a larger attenuation constant and smaller phase velocity than the corresponding diffusion in a zero ferromagnetic conductivity region.

Calculations of thrust and normal forces were made for six different SLIM models to illustrate the effect of ferromagnetic conductivity on the reaction force characteristics. The thickness of the airgap and adjacent metal region were taken as 1.5 and 3.0 mm respectively. The metal region was assumed to have an electrical conductivity of 2.5×10^7 mhos/m (AL 6061-T6 alloy). Reaction forces were computed for values of ferromagnetic thickness equal to 0.5, 3.0, and 6.0 mm and ferromagnetic conductivities of $\sigma_{iron} = 10^7$ mhos/m and zero.

The computer calculations of thrust and normal force-versus-excitation frequency are summarized in Figures 7 and 8. Curves showing computed thrust and normal force for the case of the 6.0 mm thick ferromagnetic region are omitted from the figures since their values closely followed those for the 3.0 millimeter thick case. The curves suggest some increase in reaction force magnitude is possible using a nonconducting (laminated) ferromagnetic rather than a conducting ferromagnetic. However, the relative increase in force is small for the examples chosen.

2.3.7 Computer Study of Flux Diffusion in Composite SLIM

A computer study was made to investigate magnetic diffusion along the (y) direction normal to the surface current wave in an idealized SLIM model. Six SLIM models were studied, each comprising multi-layers of air, metal, ferromagnet, and air (extending to infinity). Region 1 formed an air layer 3 millimeters thick, Region 2 a layer of metal 3 mm thick and electrical conductivity of 2.5 x 10^7 mhos/m, and Region 3 a ferromagnetic layer with thickness and electrical conductivity values given in the table below.

TABLE 2 SUMMARY OF FERROMAGNET PARAMETERS USED IN SLIM MODEL CALCULATIONS

CASE	REGION 3 (ferromagnetic)
1	d = 9mm σ = 0 mhos/m z-laminated
2	d = 9mm $\sigma = 10^7$ mhos/m nonlaminated
3	d = 3mm σ = 0 mhos/m z-laminated
4	d = 3mm $\sigma = 10^7$ mhos/m nonlaminated
5	d = 1mm σ = 0 mhos/m z-laminated
6	d = 1mm $\sigma = 10^7$ mhos/m nonlaminated

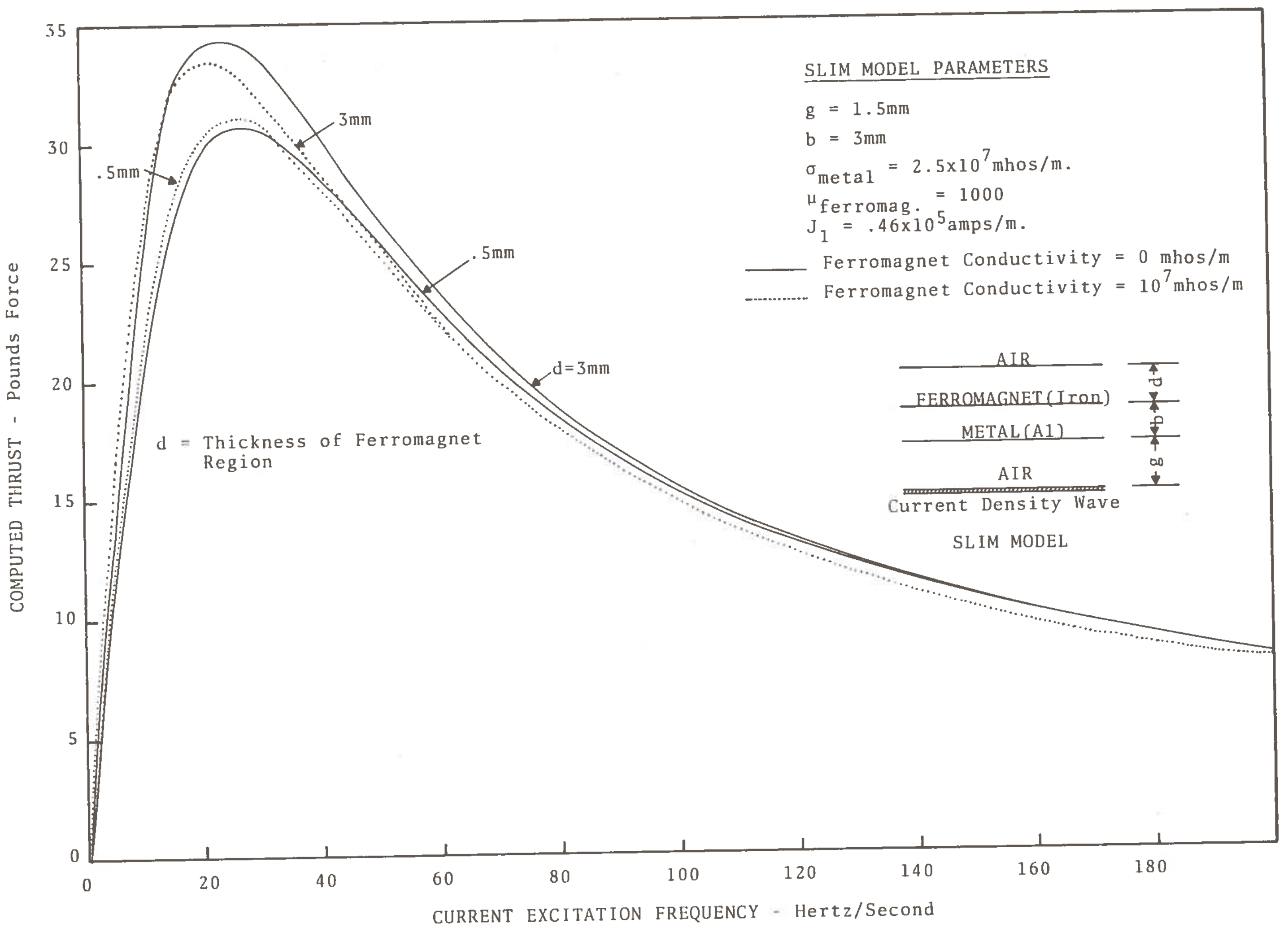

Figure 7. Computed Thrust as a Function of Current Excitation Frequency for SLIM with Laminated-Versus-Nonlaminated Ferromagnetic Backing

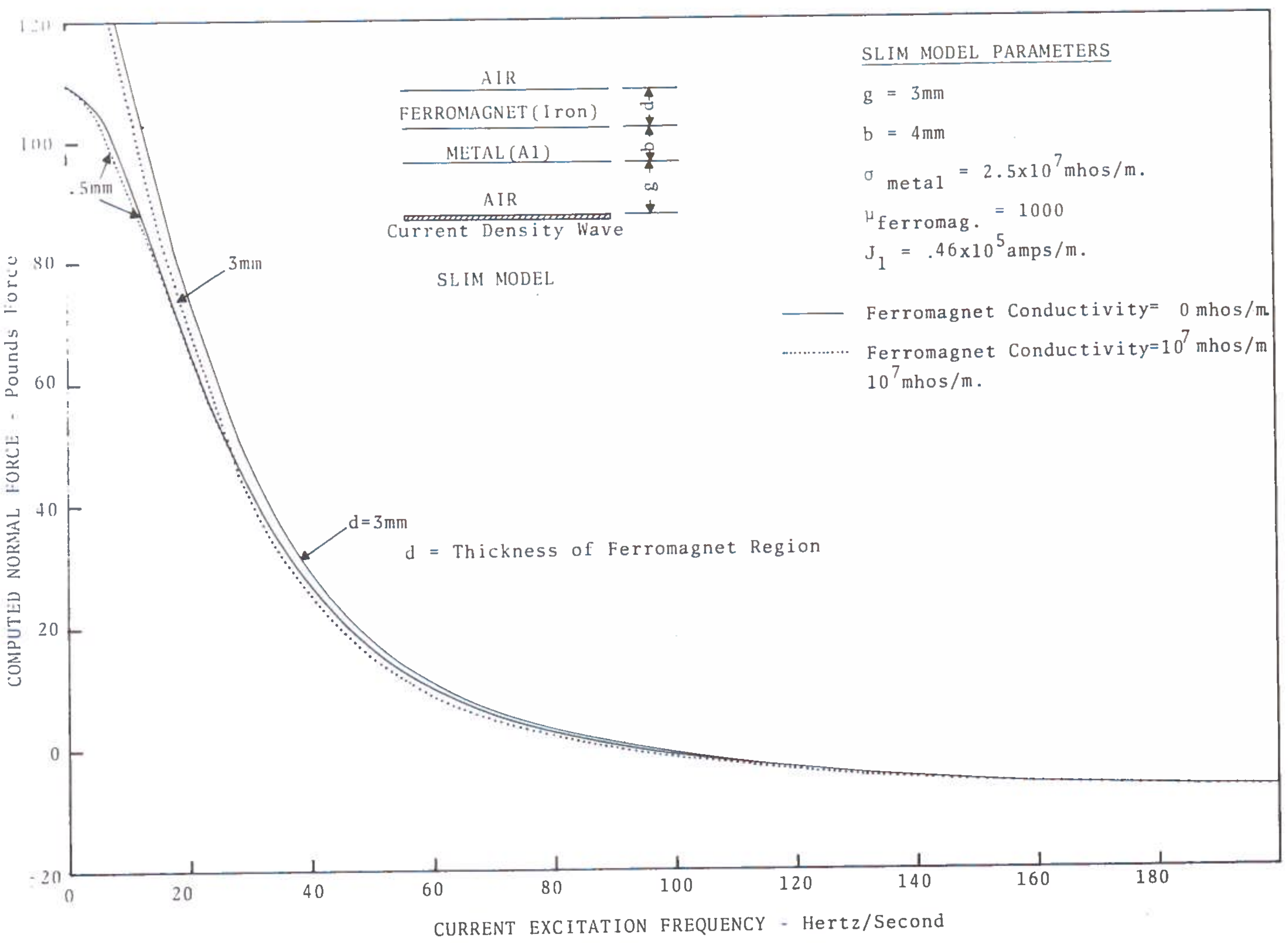

Figure 8. Computed Normal Force as a Function of Current Excitation Frequency for SLIM with Laminated-Versus-Nonlaminated Ferromagnetic Backing

The primary current excitation amplitude was taken as $J_1 = .64 \times 10^5$ amps/m corresponding to the equivalent current density for a stator phase current of 14 amperes and LIM parameters given in Table 1. Current excitation frequency was assumed constant at 40 Hz/sec.

The complex amplitudes of the normal flux density, $\hat{B}_y$, and tangential flux density, $\hat{B}_x$, were computed as a function of penetration depth along the direction normal to the primary surface current. The results of the calculations of flux density <u>amplitude</u> are shown in Figures 9 through 14; the computed <u>phase</u> of the flux density components was omitted from the figures since it was not relevant to the material discussed in this section.

A study of the different field distribution characteristics leads to a number of interesting conclusions. First, for the range of parameters considered, the flux density at the primary surface current wave remains relatively constant and independent of the ferromagnet thickness of Region 3. Thus, increasing the ferromagnet thickness from nine to one mm causes the normal flux density to change by only a few percent for both examples of ferromagnetic conductivity. Note that boundary condition (1) fixes the magnitude of the tangential flux density at the primary surface current wave. See Section 2.2.1. Second, the amplitude of the normal flux density component, B_y, in the metal and the tangential flux density component, B_x, in the ferromagnet remains relatively constant. Third, the tangential flux density component in the zero ferromagnetic conductivity region increases almost inversely with decreasing thickness of the ferromagnetic region.

A comparison of the flux plots for zero and nonzero ferromagnetic conductivity shows that larger flux densities (B_x) are developed in Region 3 for nonzero conductivity (iron plate) than for zero conductivity (laminated) ferromagnet. Consequently, magnetic saturation will occur initially with nonzero conductivity ferromagnet. For the SLIM examples corresponding to Figures 13, 14, computed flux densities (B_x) exceed the value required for onset of magnetic saturation (1.2 - 1.5 webers/ m^2). For these cases, the

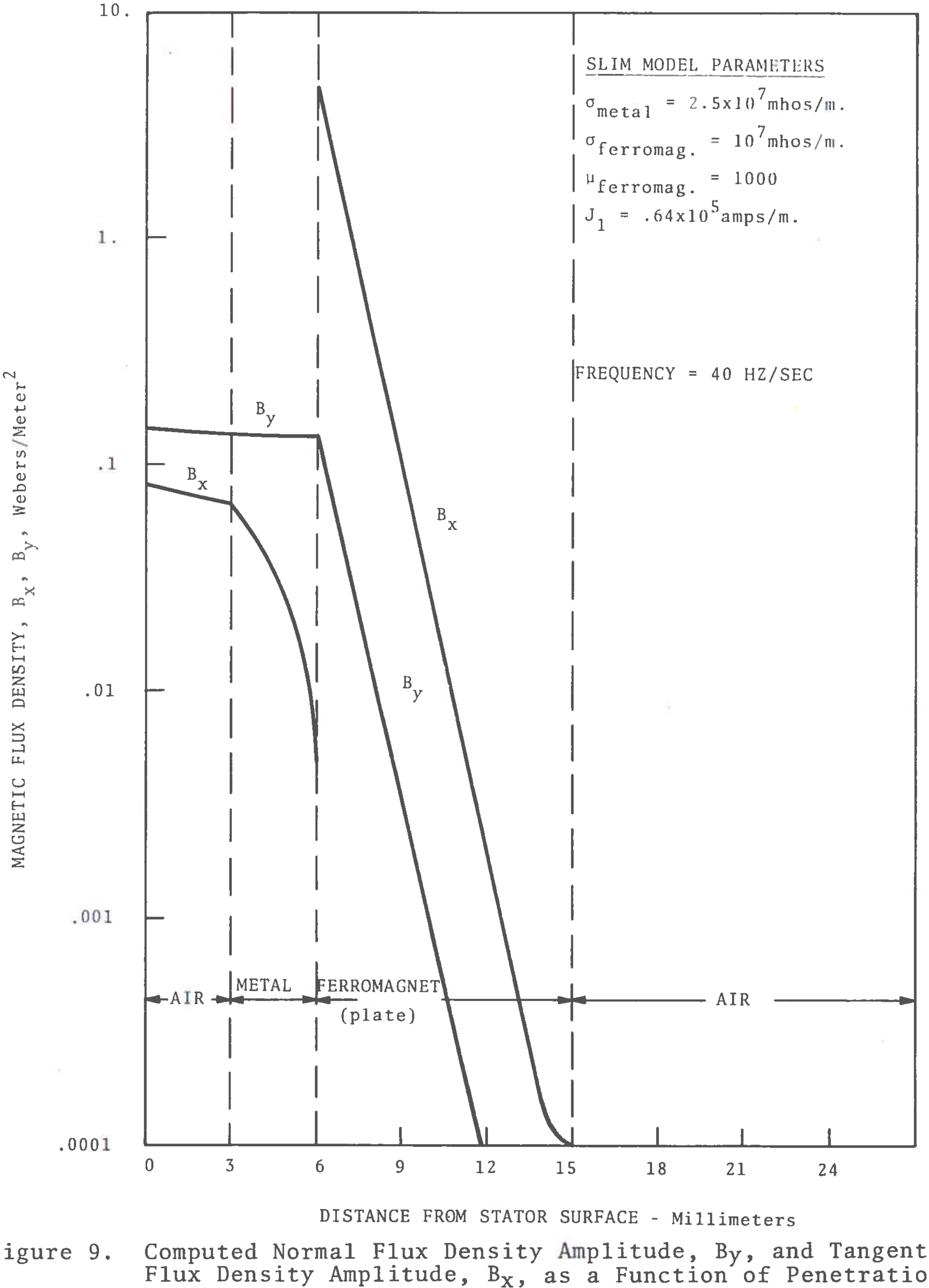

Figure 9. Computed Normal Flux Density Amplitude, B_y, and Tangential Flux Density Amplitude, B_x, as a Function of Penetration Depth in SLIM Secondary. Thickness of Ferromagnetic Region = .009 m; Electrical Conductivity of Ferromagnetic Region = 10^7 mhos/m.

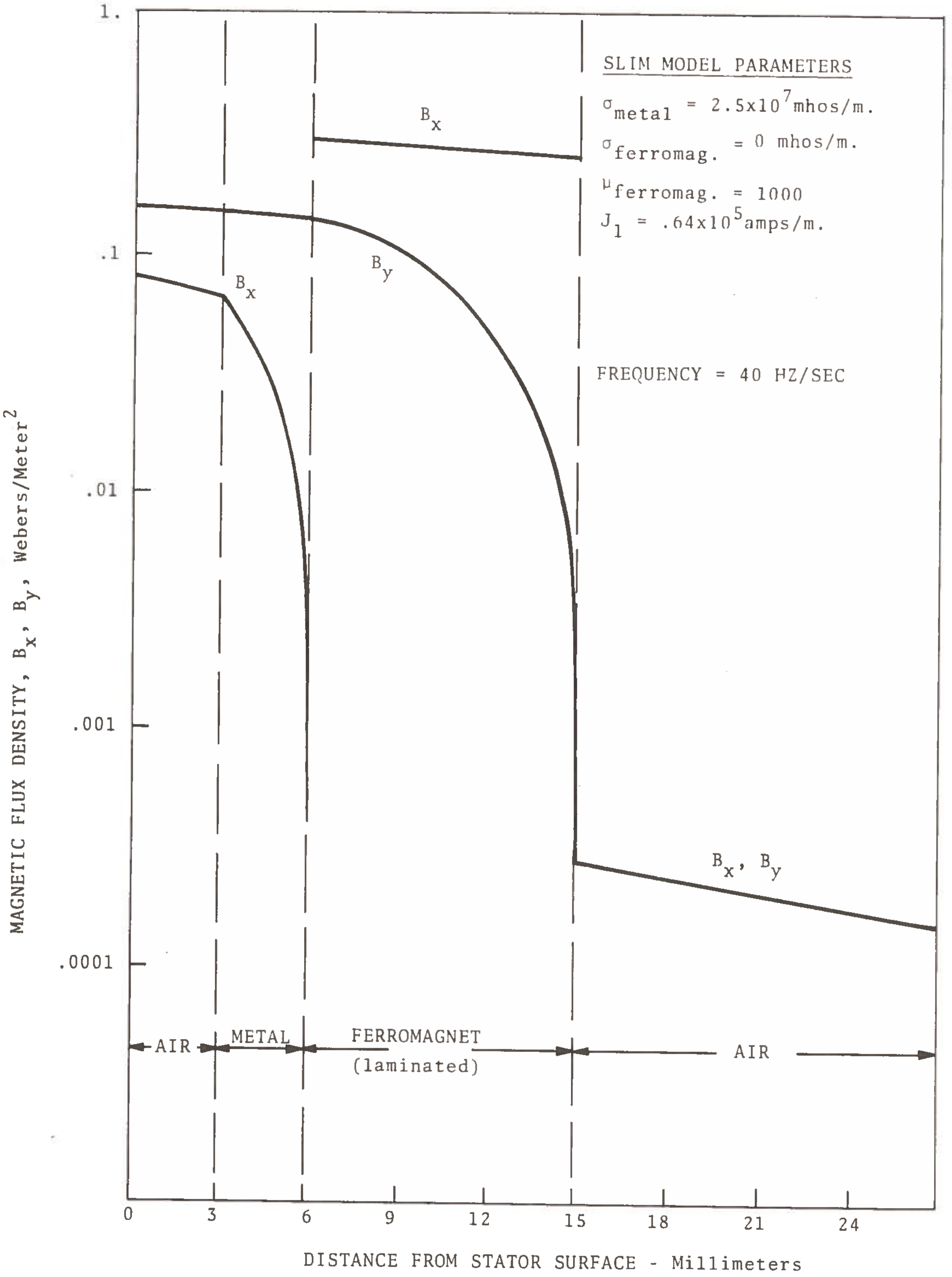

Figure 10. Computed Normal Flux Density Amplitude, B_y, and Tangential Flux Density Amplitude, B_x, as a Function of Penetration Depth in SLIM Secondary. Thickness of Ferromagnetic Region = .009 m; Electrical Conductivity of Ferromagnetic Region = 0 mhos/m.

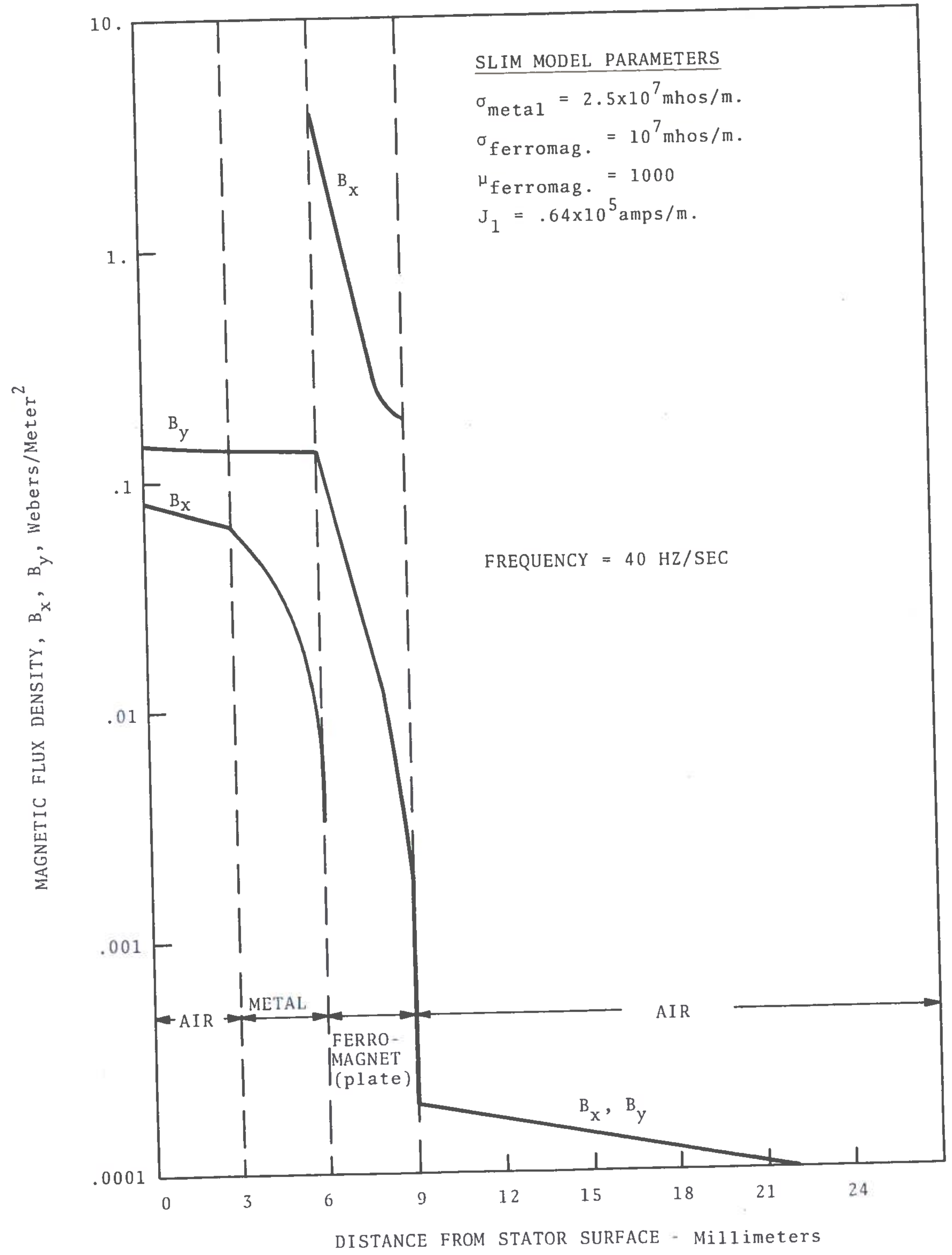

Figure 11. Computed Normal Flux Density Amplitude, B_y, and Tangential Flux Density Amplitude, B_x, as a Function of Penetration Depth in SLIM Secondary. Thickness of Ferromagnetic Region = .006 m; Electrical Conductivity of Ferromagnetic Region = 10^7 mhos/m

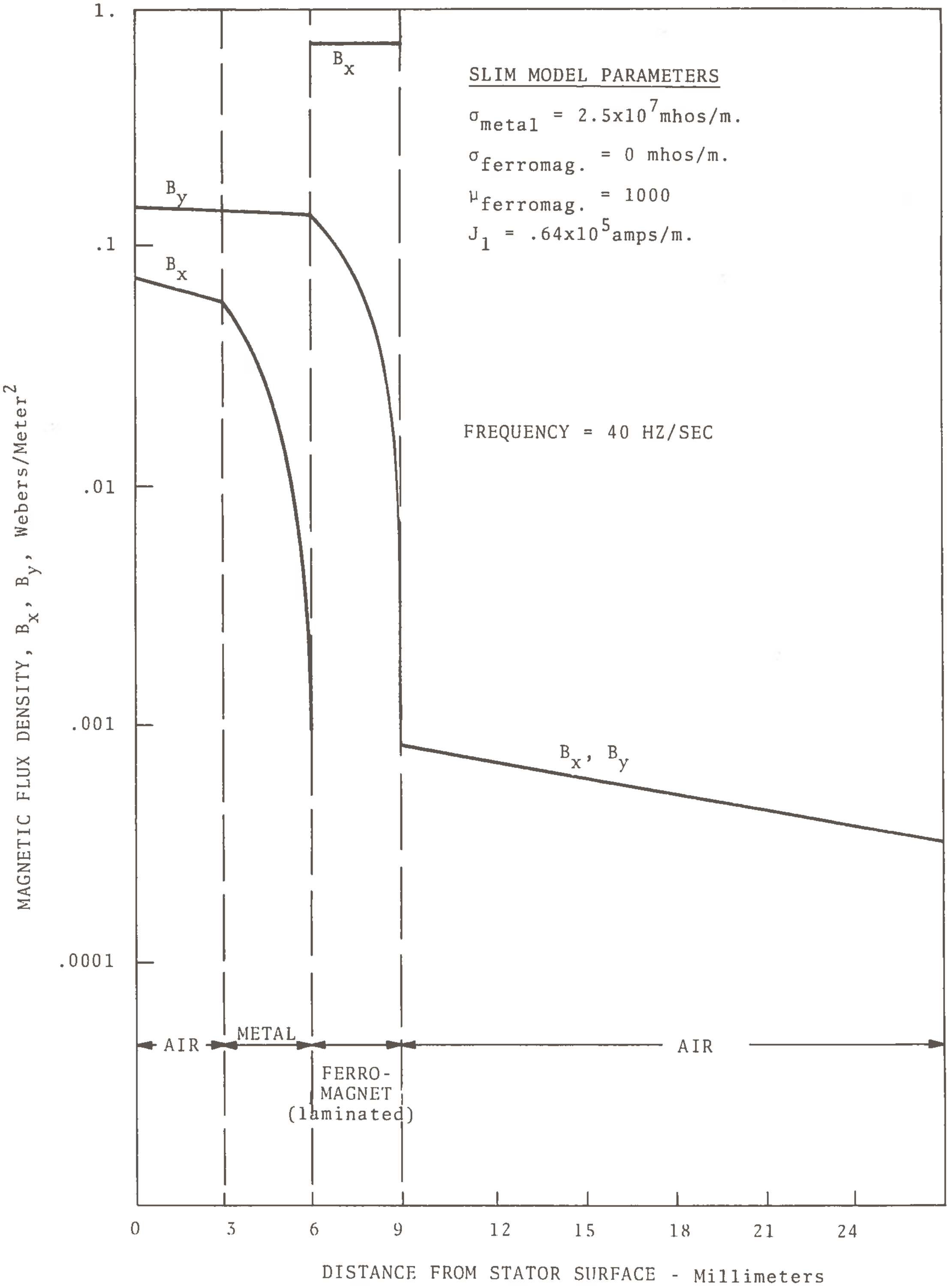

Figure 12. Computed Normal Flux Density Amplitude, B_y, and Tangential Flux Density Amplitude, B_x, as a Function of Penetration Depth in SLIM Secondary. Thickness of Ferromagnetic Region = .006 m; Electrical Conductivity of Ferromagnetic Region = 0 mhos/m

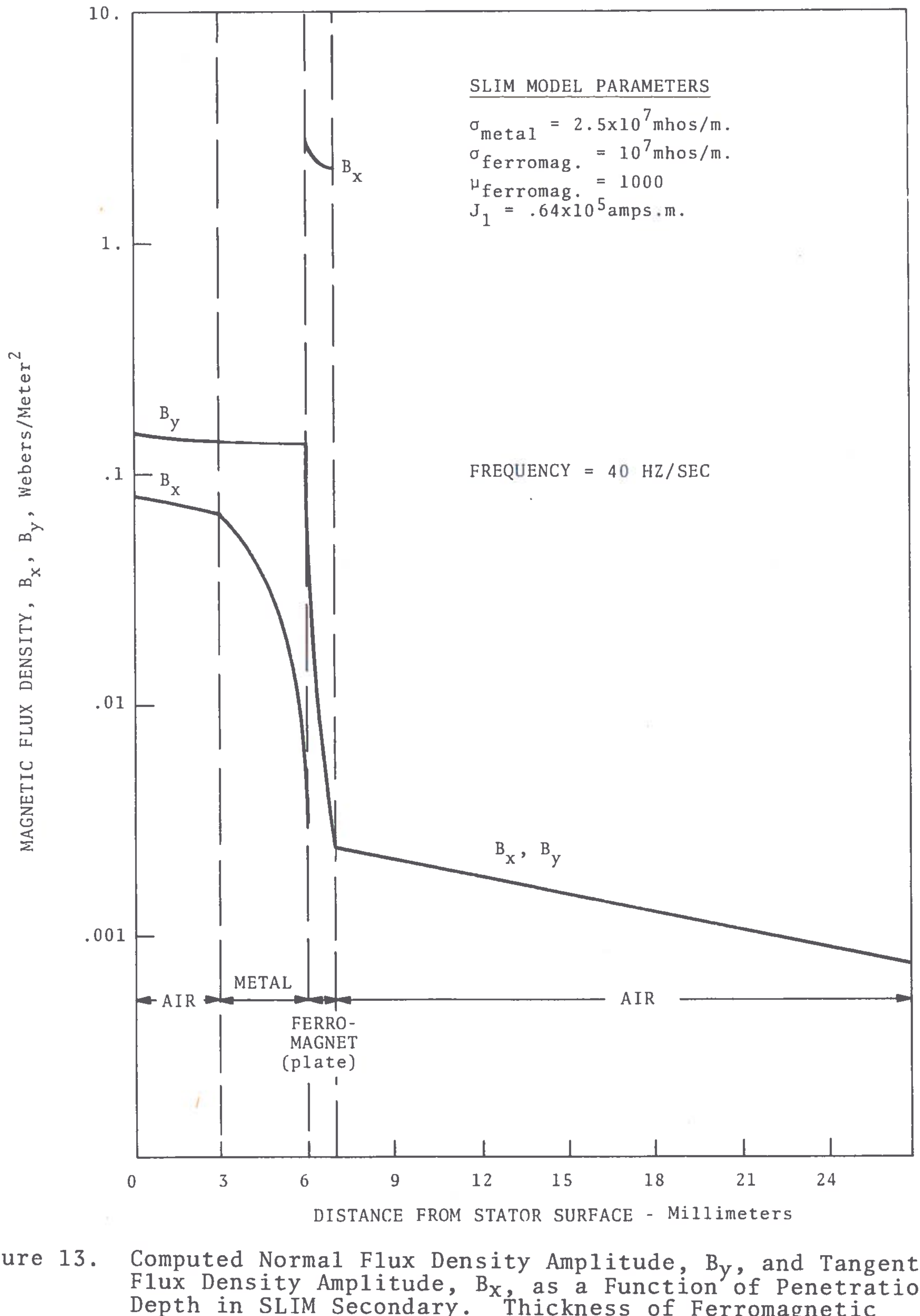

Figure 13. Computed Normal Flux Density Amplitude, B_y, and Tangential Flux Density Amplitude, B_x, as a Function of Penetration Depth in SLIM Secondary. Thickness of Ferromagnetic Region = .003; Electrical Conductivity of Ferromagnetic Region = 10^7 mhos/m

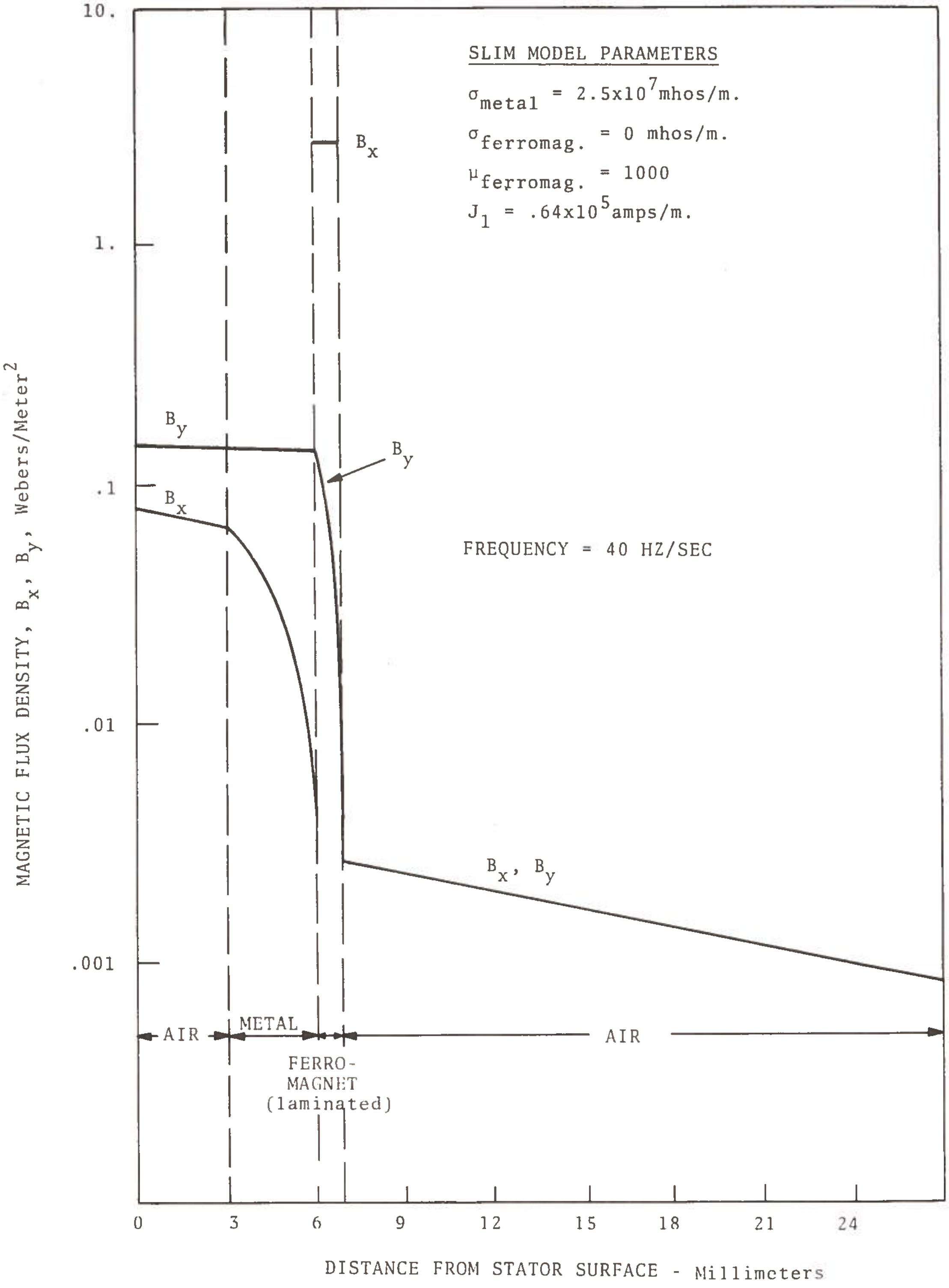

Figure 14. Computed Normal Flux Density Amplitude, B_y, and Tangential Flux Density Amplitude, B_x, as a Function of Penetration Depth in SLIM Secondary. Thickness of Ferromagnetic Region = .003 m; Electrical Conductivity of Ferromagnetic Region = 0 mhos/m

assumption of constant permeability is no longer applicable and the permeability will have a reduced value consistent with the flux density which can be supported in the ferromagnet.

2.4 EXPERIMENTAL SLIM PROGRAM

The experimental phase of the SLIM program has two principal objectives; (1) the presentation of reaction force data for different SLIM configurations and (2) the analytical correlation of empirical data with theories derived in the first part of the report. The measurements were restricted to static tests of reaction forces using a variable frequency power supply (15-200 Hz/sec) to provide data as a function of 'slip frequency'.

A photograph of the test arrangement is shown in Figure 15. For clarity in subsequent discussions, a sketch indicating the various components in the test setup is given in Figure 16. The secondary structure was clamped rigidly to the support table and reaction forces were measured on the stator relative to the support table. Three 200 lb force transducers (Schaevitz Model RTD-10-200) were positioned under the stator to support its weight and to measure the additional normal forces developed under test conditions. These transducers were positioned so that equal forces were applied to each transducer. Small metal rollers, 1/4 inch in diameter, were inserted between the transducers and stator to give translational freedom along the longitudinal axis, i.e., direction of thrust. A fourth 200 lb force transducer was located at the end of the stator to measure the thrust component of force.

The outputs of the normal force transducers under the stator were totaled using a solid-state summing circuit. The output signals from the normal force and thrust transducers were read using a dc digital voltmeter. The resolution of the test data was 0.4 pounds above 20 Hz/sec; below this frequency, the resolution was reduced by stator vibrations.

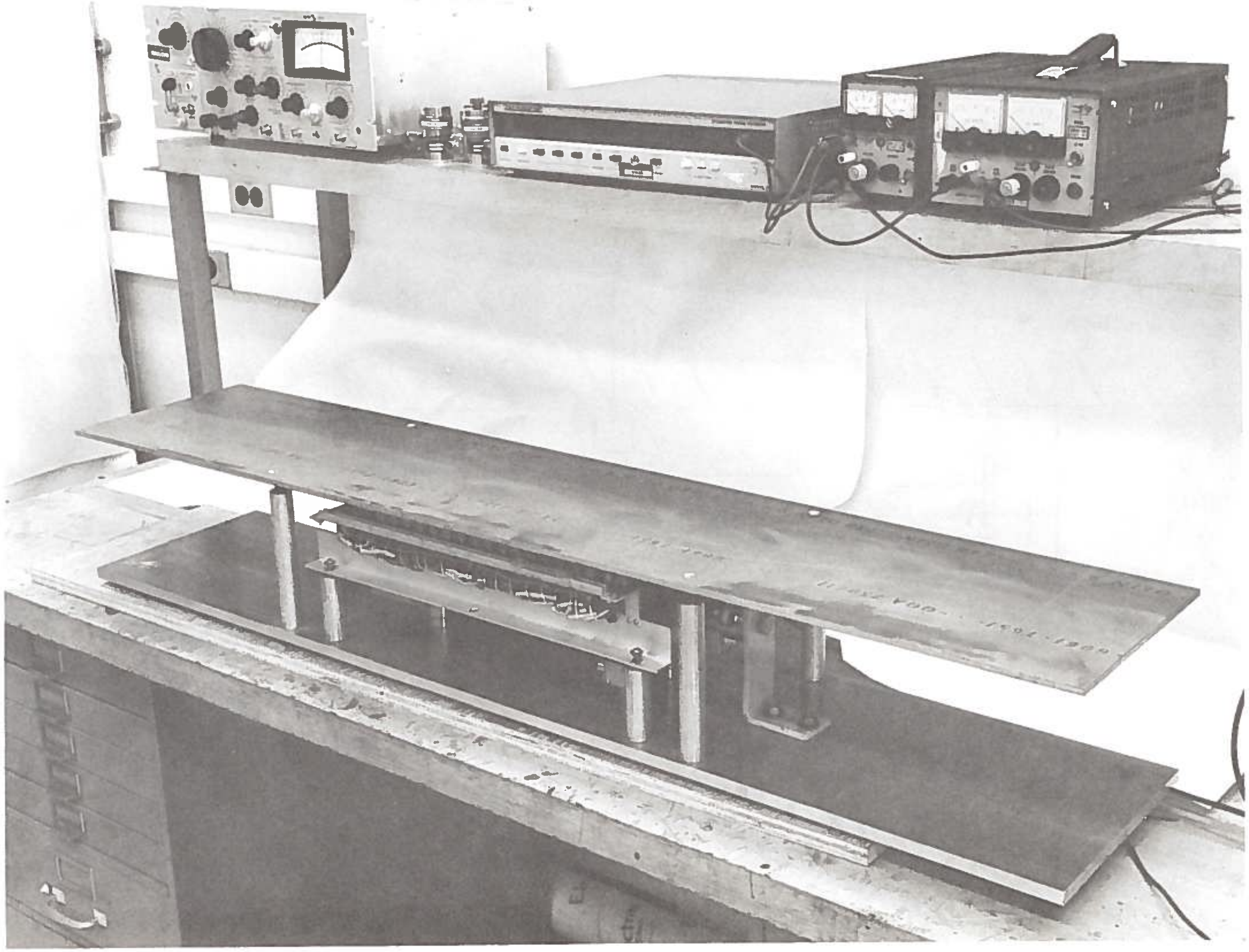

Figure 15. Photograph of Experimental Setup used for the Measurement of SLIM Reaction Forces

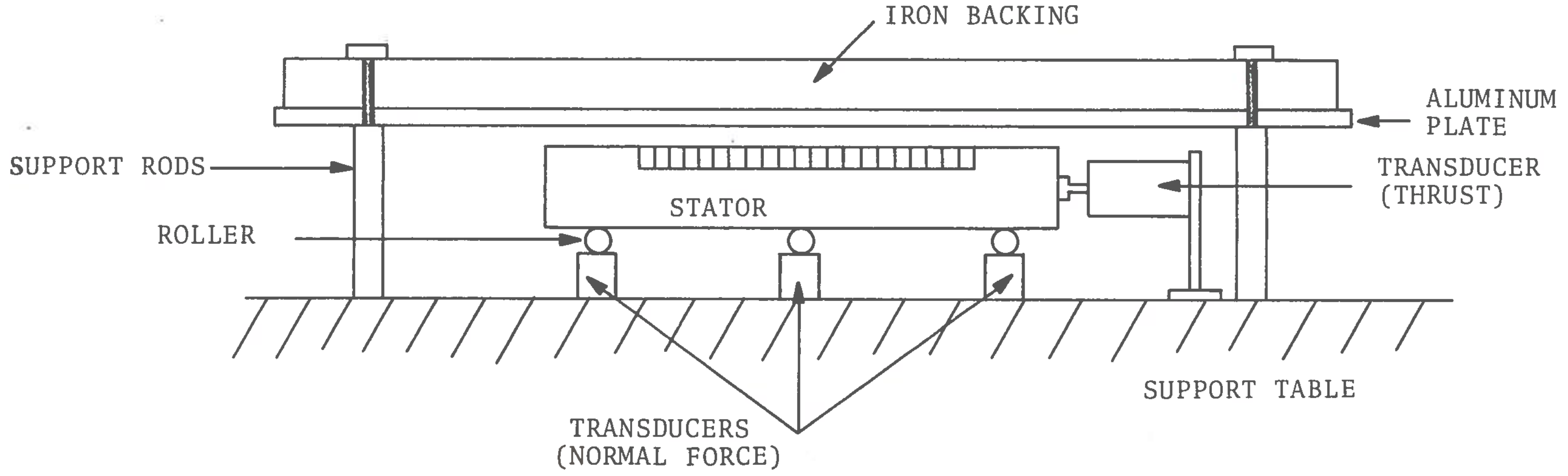

Figure 16. Sketch of Experimental Arrangement for Measuring SLIM Reaction Forces

2.4.1 Reaction Forces-versus-Thickness of Aluminum Plate Secondary

The effect of the thickness of the secondary metal region on SLIM reaction force was discussed in Section 2.2.1. Using a mathematical model which replaces the stator with a traveling current density sheet, equations were derived for flux density and reaction force as a function of excitation frequency and secondary region (Region 2) thickness. In this section, the results of laboratory tests made with various thickness aluminum plate secondaries are presented. Figure 16 shows a sketch of the test arrangement. The secondaries were formed of aluminum alloy (6061-T6) plates 10 inches wide and thicknesses varying from 1/8 to 1 1/8 inches.

The thrust-versus-stator current excitation frequency measured for three secondary specimens is shown in Figure 17. The frequency of maximum thrust varied almost inversely with secondary plate thickness as predicted by Equation (28). For the 1 1/8 inch thick secondary, maximum thrust occurred at 30 Hz/sec which compares with the computed frequency of 27.8 Hz/sec given by Equation (31) for an infinitely thick secondary. The 1/8 inch thick secondary gave maximum thrust at a frequency near 100 Hz/sec which compares with the computed frequency of 106 Hz/sec predicted by Equation (28).

The thrust characteristics computed using the finite-thickness secondary model described in Section 2.3.1 is also presented in Figure 17. The current density used in the calculations was $J_1 = 0.64 \times 10^5$ amps/m. (Note, this is equivalent to a phase current of 14 amperes for the stator parameters given in Table 1). Airgap distance was taken as .001 m. The correlation of measured and computed thrusts is good for the 1/4 and 1 1/8 inch thick secondaries but only fair for the 1/8 inch thick secondary. In the latter case, measured thrusts are about twenty percent lower than the thrusts computed using the finite-thickness model.

The SLIM examples with 1/8 inch and 1 1/8 inch thick secondaries are representative of SLIMs operated with different modes of secondary current flow. In the first case, the secondary plate thickness is less than the skin depth over the range of frequencies measured. (At 1 KHz/sec, skin depth equals plate thickness.)

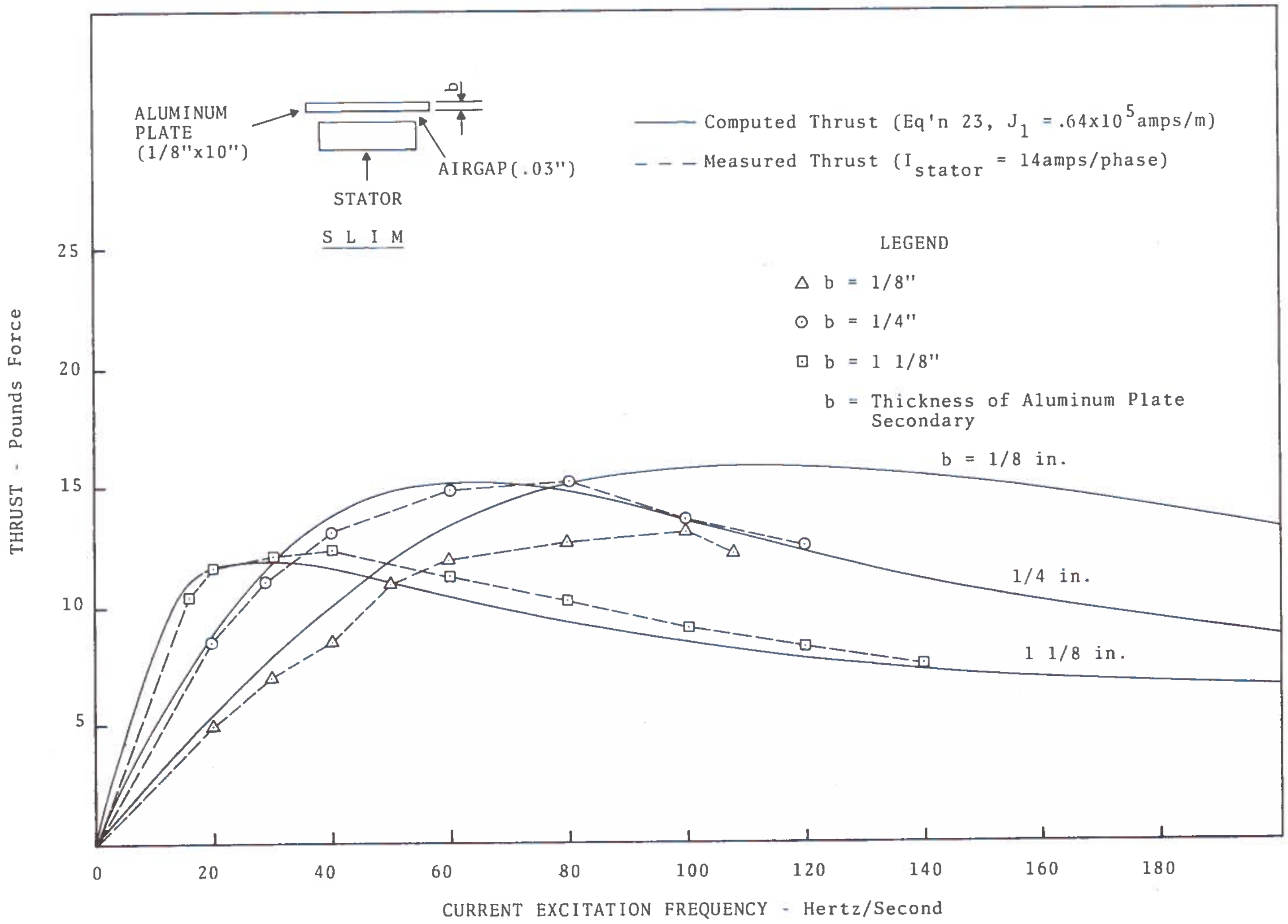

Figure 17. Measured SLIM Thrust-versus-Current Excitation Frequency for Different Thicknesses of Aluminum Secondary

The secondary current must flow principally in the (xz) plane of the secondary and give rise to x-directed edge currents as required for current continuity. In the case of the 1 1/8 inch thick secondary, the plate thickness exceeds the skin depth for excitation frequencies above 12 Hz/sec. Above this frequency, edge current flow (xz plane) will be subordinate to eddy current flow (xy plane). The SLIM model presented in the first part of this report, i.e., Section 2.3.1, which is based on eddy current flow in the secondary, should more accurately describe a SLIM with thick secondary (example with 1 1/8 inch secondary plate) than a SLIM with thin secondary (example with 1/8 inch secondary plate). The thrust characteristics given in Figure 17 are consistent with this conclusion.

Previous analyses have shown that secondary edge currents in the SLIM act to reduce the net thrust by decreasing both the effective secondary conductance and effective primary excitation current (10, p. 141). While comparable analyses of edge-effect phenomena in SLIMs are lacking, it is reasonable to expect a similar reduction in SLIM thrust due to edge currents in the secondary. A second contributing factor to thrust reduction is the presence of higher-order flux harmonics which interact with z-directed secondary currents. A discussion of the combined effect of these factors as it relates to the data shown in Figure 17 is beyond the scope of this report.

The normal force characteristics measured with 1/8, 1/4, and 1 1/8 inch thick secondaries are shown in Figure 18. All measured forces were repulsive and increased in magnitude with stator excitation frequency. The SLIM normal forces with the 1/4 and 1 1/8 inch thick secondaries approached an asympototic limit of 18 to 20 pounds at the higher frequencies. The SLIM normal force with the 1/8 inch thick secondary was considerably less than that measured for the other two SLIMs.

The normal forces computed using the finite-thickness SLIM model are indicated by the dashed curves in the figure. The assumed fictitious current density used in the calculations was

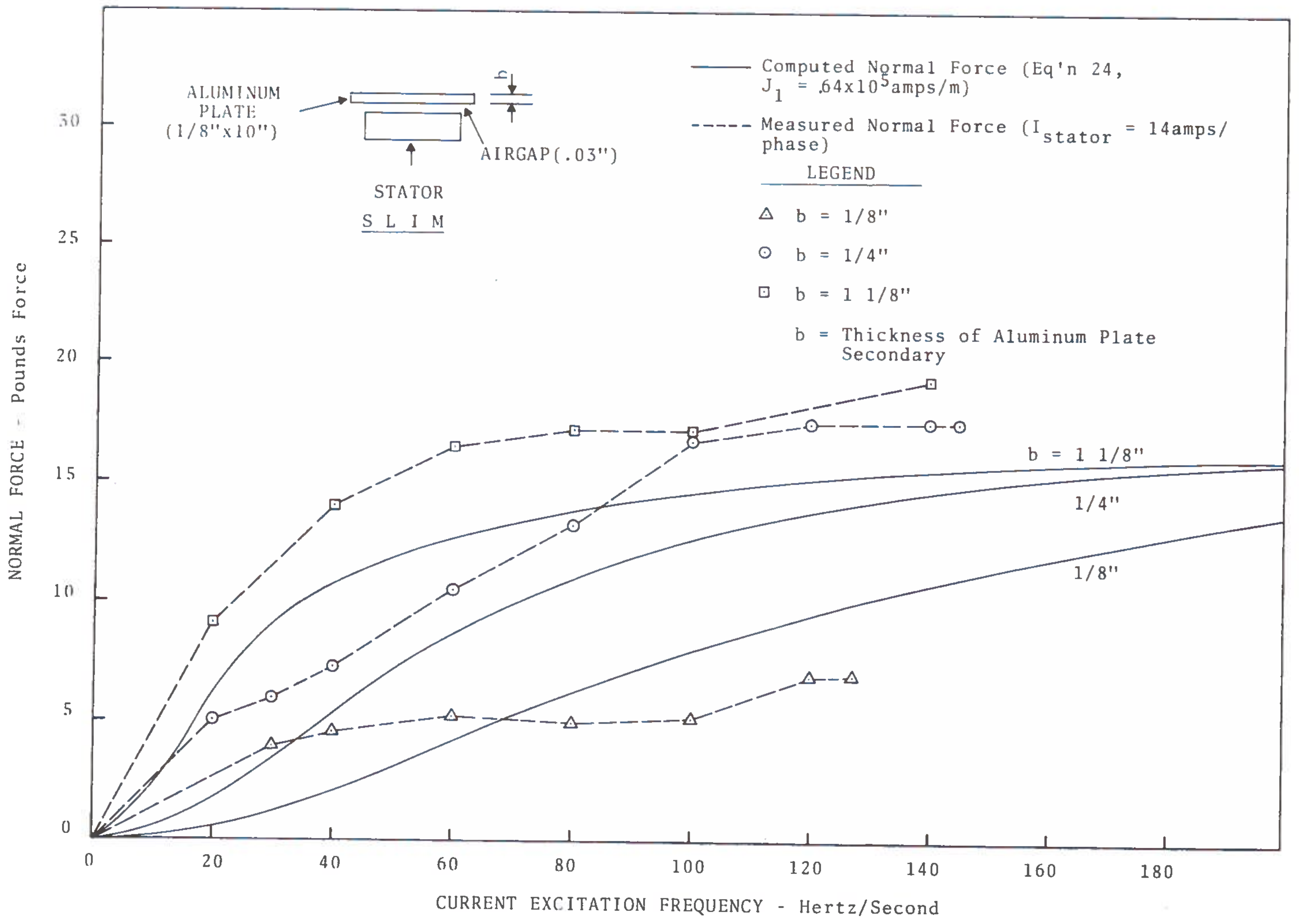

Figure 18. Measured SLIM Normal Force-versus-Current Excitation Frequency for Different Thickness of Aluminum Secondary. Dashed Curves give Computed Normal Force based on Idealized Mathematical SLIM Model

$J_1 = .64 \times 10^5$ amps/m, and the airgap separation distance was $g = .001$ m. While this latter value was slightly larger than that used in the tests, the error introduced was not considered significant.

The shape of the computed normal force characteristics for 1/4 and 1 1/8 inch thick secondary regions was similar in form but of reduced magnitude compared with the measured normal force characteristics. The normal force characteristic for the 1/8 inch thick SLIM secondary exhibited a different functional dependence on excitation frequency. The quadratic frequency dependence predicted by theory was not observed in the lower frequency range.

The previous discussion of edge-effect on SLIM thrust must also be applicable to the treatment of the normal forces in the SLIM. Correlation is realizable for the 1/4 and 1 1/8 inch thick secondary SLIMs if the fictitious current density used in the SLIM model is increased ten percent. The correlation of the 1/8 inch thick SLIM presents another problem. If edge currents are responsible for the difference between measured and computed normal forces in this case, the data suggests that the edge-effect forces must have a frequency dependence opposite to that associated with the normal traveling wave. Additional studies would be helpful in providing a better understanding of these factors.

2.4.2 Composite SLIM Reaction Force-versus-Width of Iron Backing

Previous studies of SLIM reaction forces were restricted to SLIMs with aluminum-only secondaries. The remainder of this report will be devoted to studies of composite SLIMs with aluminum-iron backing secondaries. The data presented in this section describes the dependence of SLIM reaction force on the width of iron backing.

The schematic of the test setup is shown in Figure 16. The SLIM secondary comprised 1/8" x 10" aluminum (6061-T6) alloy plate with iron backing formed of various width specimens of Type 1018 cold drawn steel, 1/4 inch thick. The steel backing plates varied in width from 2 to 10 inches. The secondary structure was positioned parallel to the stator surface and separated from it by an airgap spacing of 5/32 inch. Stator current was maintained constant at 10 amps RMS.

The test results of SLIM thrust-versus-frequency are shown in Figure 19 for the different secondary specimens. The increase in thrust produced by the back iron (steel) is seen by comparing the lower curve for the SLIM without iron backing with the other curves for the SLIM with iron backing. The peak thrust measured with the 8 inch wide backing occurred at 40 Hz/sec and had an amplitude about seven times larger than the thrust measured without iron backing.

The test results for the normal force-versus-frequency are given in Figure 20 for the different widths of the iron backing secondaries. The large attractive normal force caused by the presence of iron backing is seen by comparing the data in the lower curve for no iron backing with the data in the remaining upper curves. Below 80 Hz/sec, the attractive force dominates the repulsive force and the net force is attractive. The variation of normal force with frequency is consistent with the functional dependence of F_y on frequency predicted by Figure 6. At higher frequencies, the curves for different backing widths converge asymptotically to the curve for zero backing. The magnitude of normal force at low frequencies and the frequency of the zero force crossing both vary with width of iron backing. For the 8 inch backing width specimen, the zero crossing frequency is about 20 percent greater than that indicated in Figure 6.

Figure 21 shows the thrust and normal forces as a function of the width of iron backing measured at the stator excitation frequency of 40 Hz/sec. While larger back iron widths produce increased thrust and normal forces, the rate of increase falls off for back iron widths exceeding the stator width (7"). It is estimated from the data given in Figure 21 that the thrust for a back iron width equal to the stator width is approximately 85 percent of the value which would obtain for a back iron region of unlimited width.

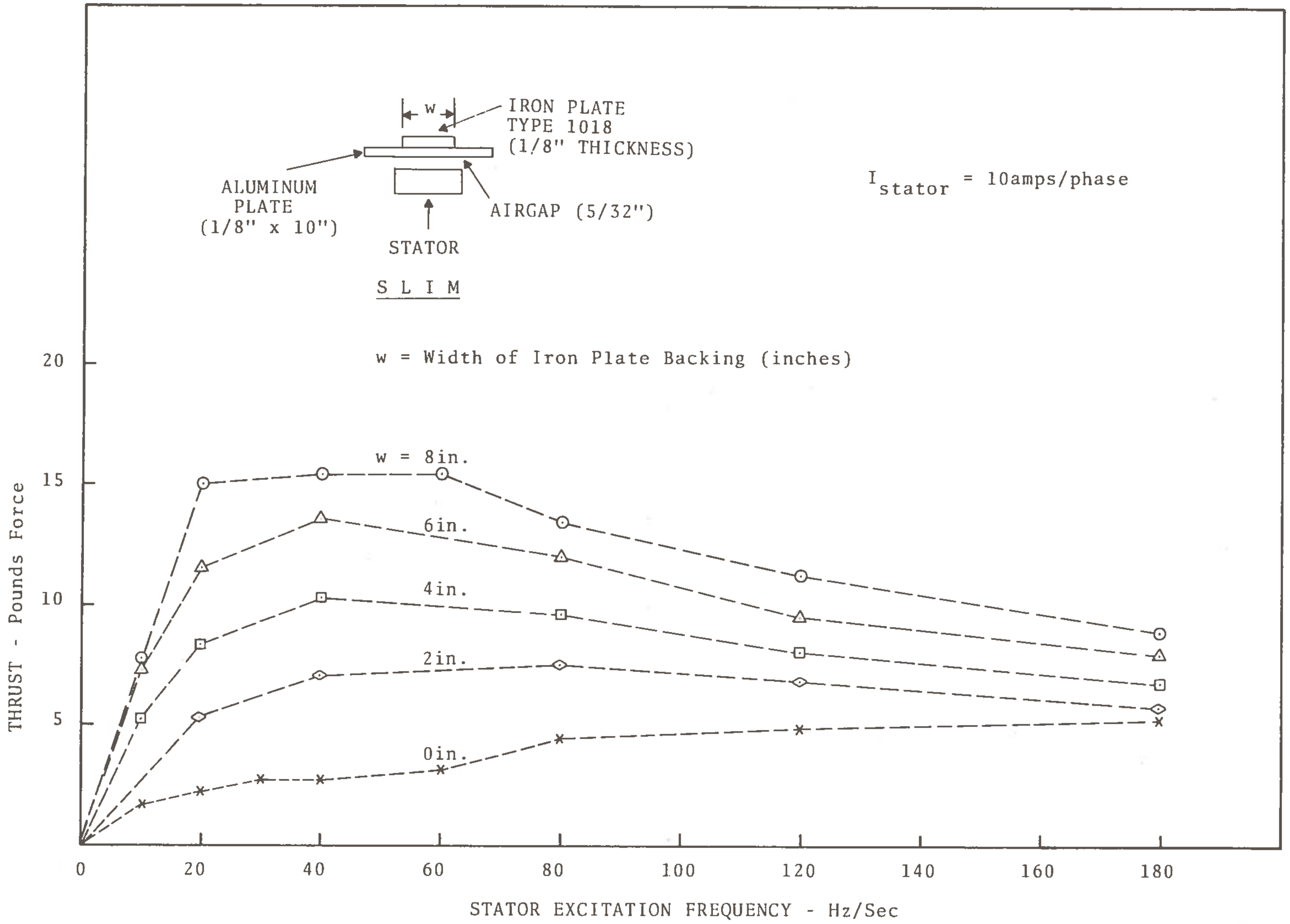

Figure 19. Measured SLIM Thrust-versus-Stator Excitation Frequency for Different Widths of SLIM Iron Plate Backing

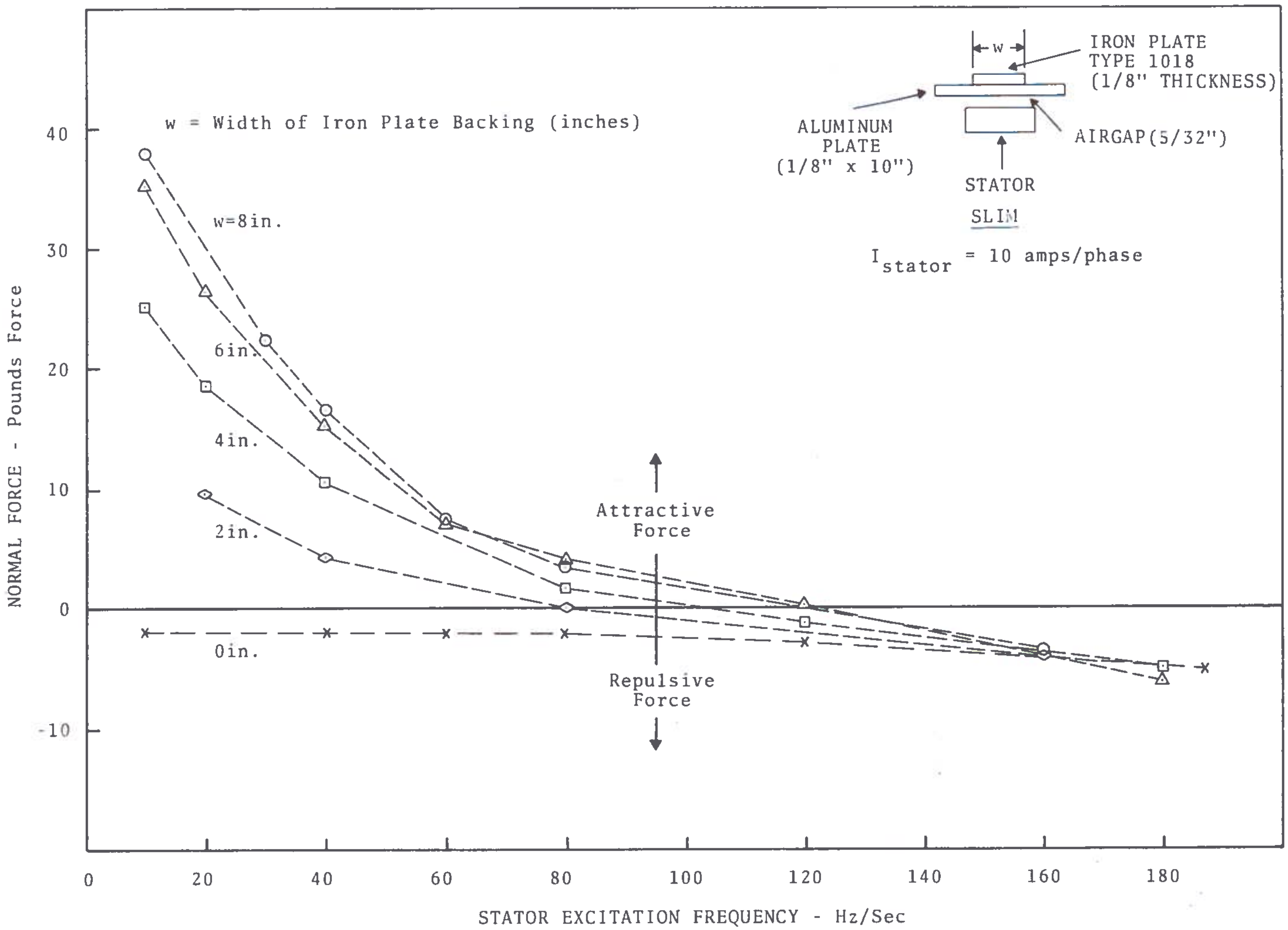

Figure 20. Measured Normal Forces-Versus-Stator Excitation Frequency for Different Widths of Iron Plate Backing

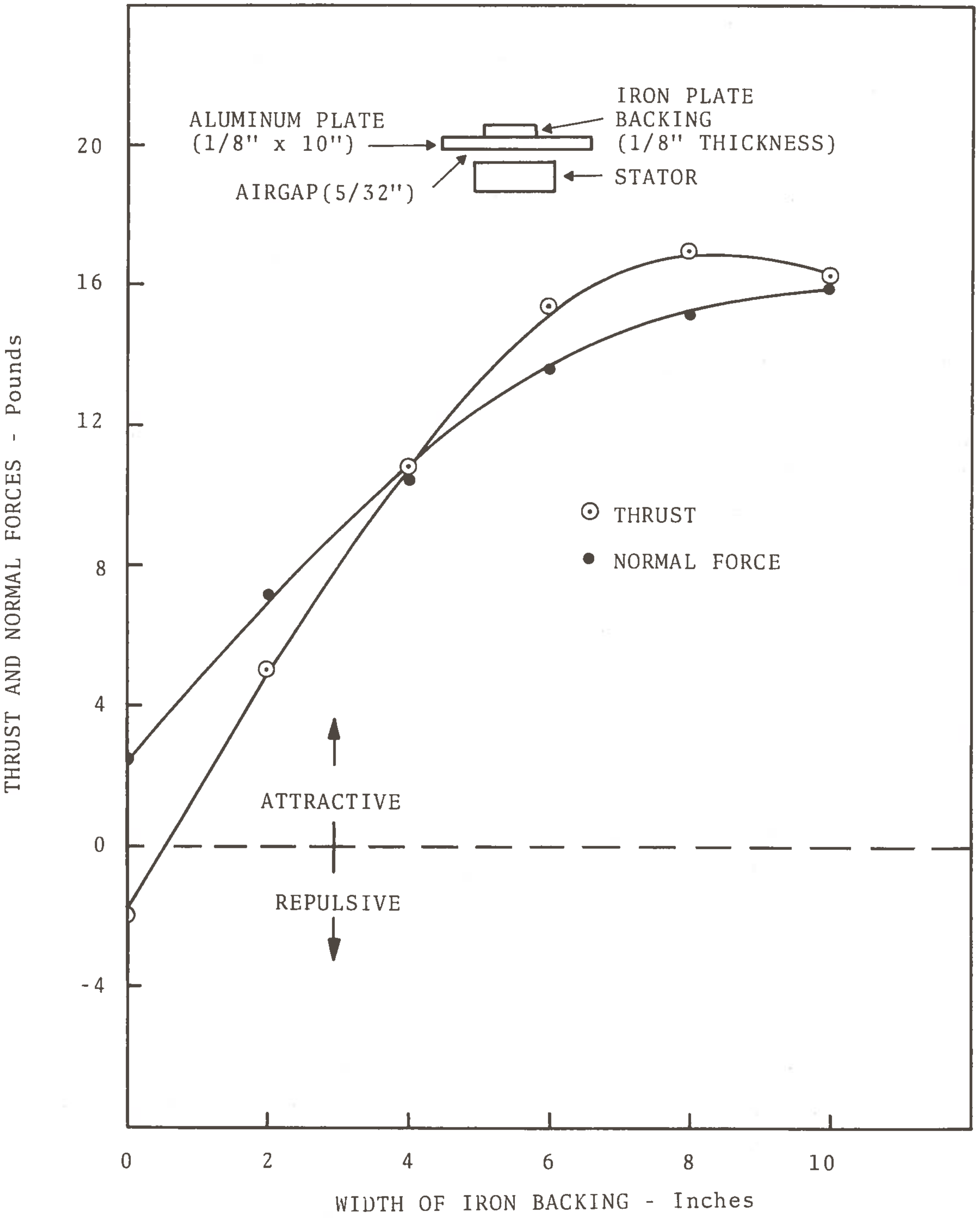

Figure 21. Measured SLIM Thrust and Normal Forces-versus-Width of Iron Backing in Composite Secondary

2.4.3 Composite SLIM Reaction Force-versus-Thickness of Iron Backing

The dependence of SLIM reaction forces on iron backing thickness of composite SLIMs was next investigated. These studies had three purposes: (1) to provide quantitative data for correlation with mathematical solutions of hypothetical SLIM models, (2) to provide empirical data relating SLIM performance to thickness of iron backing, and indirectly to establish a minimum back iron thickness for effective SLIM operation, and (3) to examine possible magnetic saturation effects associated with thin back iron secondaries.

The reaction force tests were conducted with different thicknesses of Type 1018 steel plate positioned on the back surface of a 1/8" x 10" aluminum alloy (6061T6) plate. All steel backing samples were 8 inches in width. Thrust and normal forces were measured at a stator current of 10 amps and airgap separation distance of 5/32 inches.

Figure 22 summarizes the data on SLIM thrust measured as a function of stator excitation frequency. The measured thrust in the absence of iron (steel) backing is indicated by the lower curve. The increase in thrust produced by iron backing is substantial and at 40 Hz/sec, amounts to a factor of seven.

The data shows back iron thickness greater than 1/8 inch produced little additional increase in thrust. At frequencies below 30 Hz/sec, some increase in measured thrust obtains with thick iron backing specimens, e.g., 1/2 inch specimen. From a practical standpoint, however, the choice of back iron with thickness in the range 1/16 to 1/8 inch represents a reasonable compromise for the test SLIM operated with a 1/8" x 10" aluminum secondary.

Test data obtained with a monolayer of gage 26 M-19 steel placed on the aluminum alloy secondary is also presented in Figure 22. The results are particularly interesting since the thrust characteristic gives evidence of magnetic saturation at frequencies below <u>100</u> Hz/sec. Supplemental magnetic saturation studies with multi-layer thicknesses of gage 26, M-19 steel backing demonstrate the onset of saturation with two layers of gage 26 (.037" thick) at

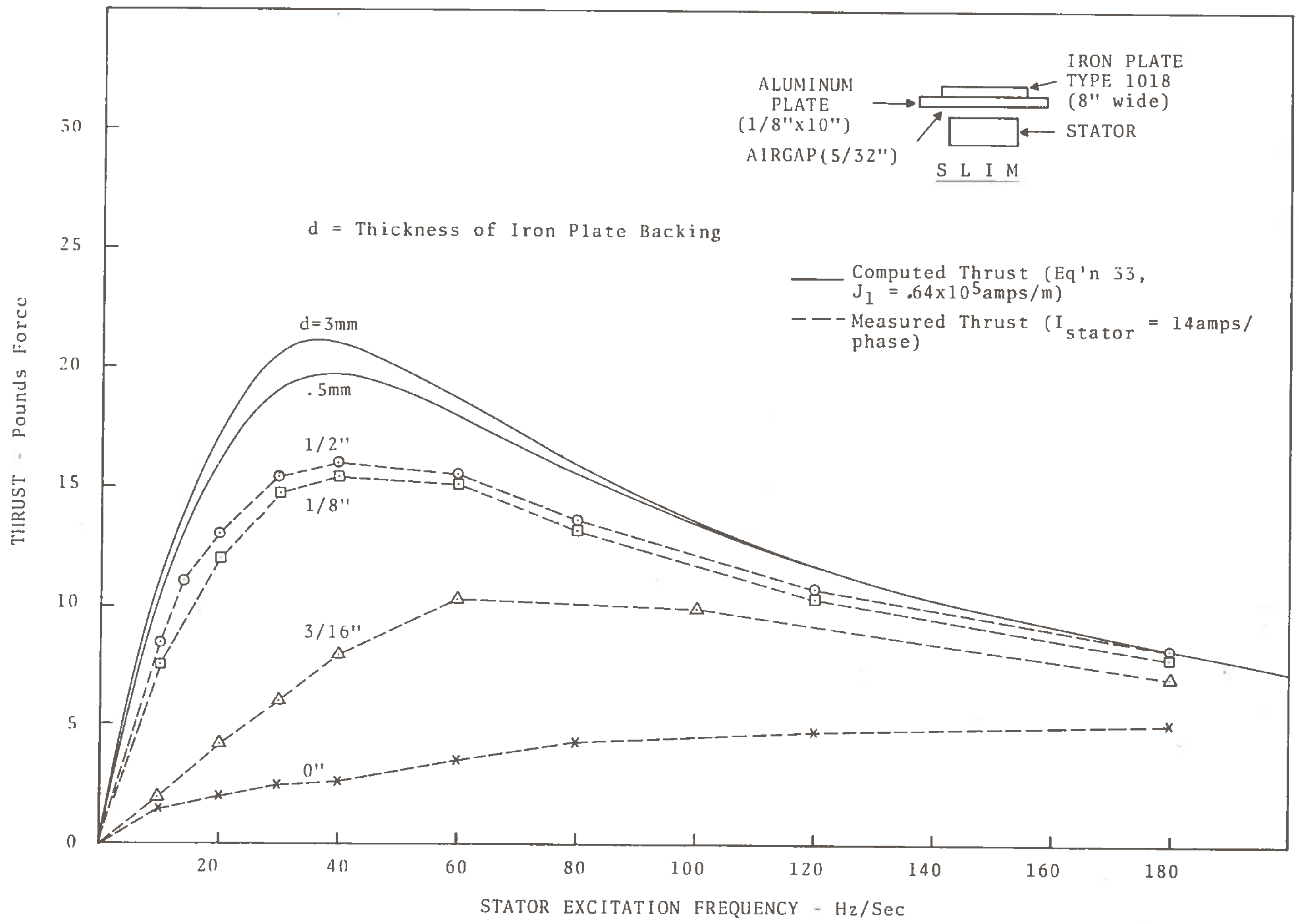

Figure 22. Measured Thrust-Versus-Stator Excitation Frequency for Different Thicknesses of Secondary Iron Plate Backing

10 amps stator current and a frequency of 40 Hz/sec. The magnetic saturation of the monolayer iron backing in the low frequency range alters the form of the thrust characteristic and causes a shift in peak thrust towards higher frequencies.

The peak thrust which occurs at 40 Hz/sec for thick iron backing shifts to near 80 Hz/sec when the iron backing is reduced to the thickness of one lamination of 0.0185 inches. The computer flux distribution studies presented in Section 2.3.7 showed that if magnetic saturation effects are neglected, the computed thrust is not reduced significantly when the thickness of the back iron region is decreased to one millimeter. This collaborates the conclusions of the experimental tests which indicate that magnetic saturation and not skin depth phenomena is responsible for the reduction in thrust observed in Figure 22 for back iron thickness less than .055 inches.

The theoretical thrust-versus-frequency characteristics computed on the basis of the mathematical model of a finite thickness conducting sheet with finite thickness iron backing outlined in Section 2.3.4 are indicated by the dashed curves shown in Figure 22. The calculations were made using the following SLIM parameters: 4 mm airgap spacing; 3 mm aluminum plate thickness; 3 mm iron backing thickness. There is an appreciable loss in the measured thrust, compared with the computed thrust in the low frequency range below 80 Hz/sec. At frequencies above 120 Hz/sec, computed and measured thrust are in good agreement. The maximum deviation occurs near 30 Hz/sec with the computed thrust being about 30 greater than the measured thrust.

A discussion of the factors responsible for deviations between theory and measured SLIM thrust should include edge effects, higher-order flux harmonic, magnetic saturation, and errors involved in estimating the fictitious current amplitude used in the computer calculations. In regard to the latter effect, an overestimate of the primary current density amplitude by 15 percent would account for the discrepancy between theory and measurement. Edge currents in the secondary have been shown by Yamamura (10, p. 142) (following the analysis of Bolton((5) to cause a reduction in thrust by an amount which increases with slip frequency. This is in a direction opposite to that required to improve agreement between theory and experiment. The effect of higher-order flux harmonics could be important. Flux mapping studies (to be published) have shown that the principle slot harmonic has an amplitude about one-third that of the fundamental; the fundamental flux harmonic must, therefore, be significantly less than it would be in the absence of the higher-order harmonics. A reduced fundamental flux amplitude, or equivalently a reduced primary current excitation amplitude, is in the correct direction to improve agreement between theory and experiment. The possibility of magnetic saturation of back iron is discounted since the data shows little divergence between measured SLIM thrust for the 1/8 and 1/2 inch thick secondaries.

It is interesting to compare the predicted frequency for maximum thrust, using Equation (28) (thin-sheet approximation), with the measured frequency given in Figure 22. For g = .004m, b = .003m, the predicted frequency of maximum thrust is 36 Hz/sec which compares with the observed value of 40 Hz/sec.

The SLIM normal force as a function of stator excitation frequency is presented in Figure 23 for the different thicknesses of back iron. The lower curve shows the measured force in the absence of back iron. The addition of iron backing produced an attractive component of normal force which at low excitation frequencies is an order of magnitude larger than the repulsive component. This implies that for railway applications requiring vehicle suspension, the utilization of attractive forces rather tham repulsive forces would be more effective in developing the magnitudes of forces necessary for vehicle suspension.

A comparison of the normal force characteristic for 1/8 inch iron backing with that for 1/2 inch shows that little there is increase in normal force due to added thickness of iron backing. This result supports the conclusion that a 1/8 inch thick iron backing is optimum for the SLIM when operated under conditions

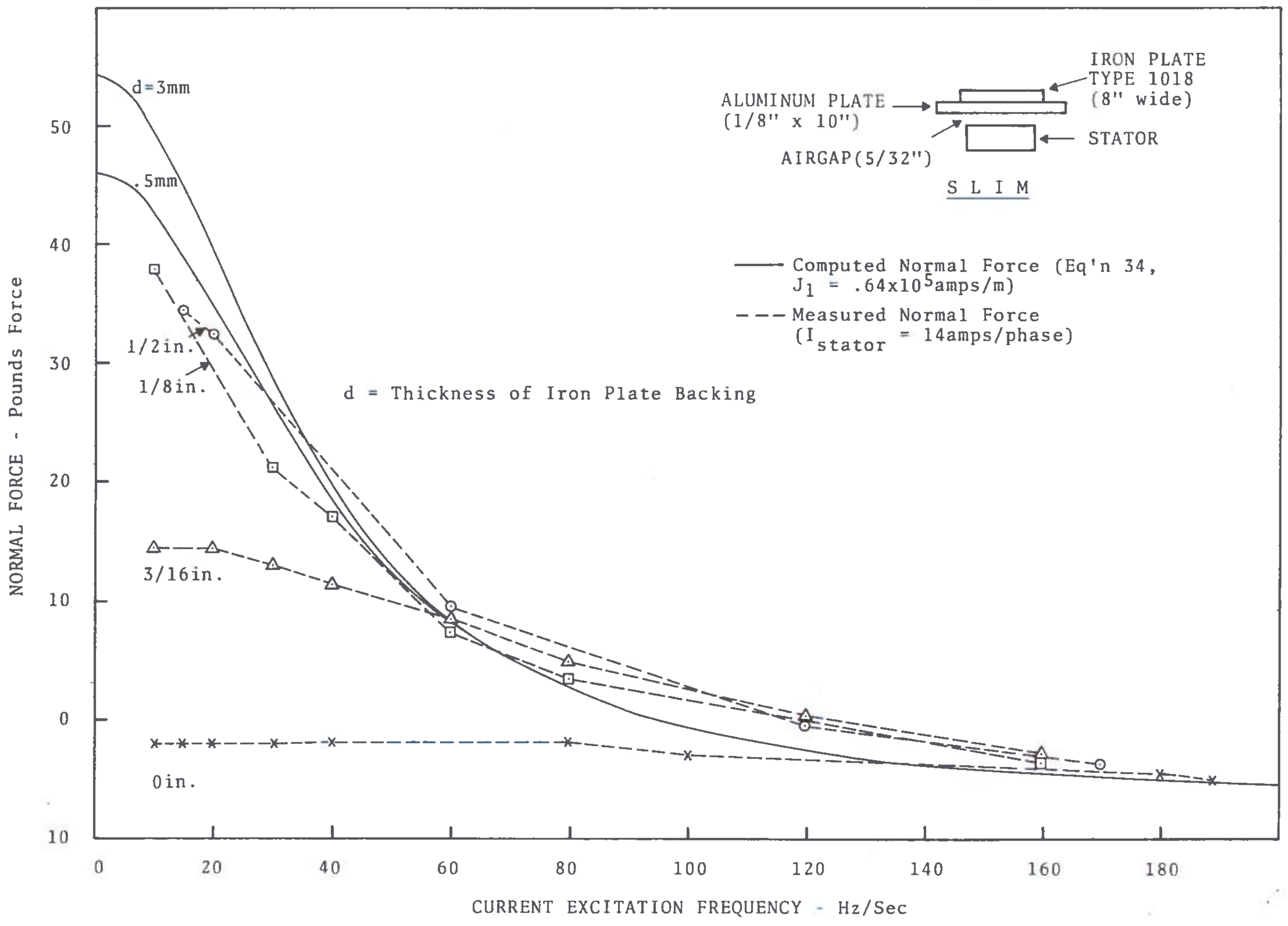

Figure 23. Measured Normal Force-Versus-Stator Excitation Frequency for Different Thicknesses of Secondary Iron Plate Backing

The data for back iron specimens comprising one and two layers of Gage 26, M-19 iron illustrate the effect of magnetic saturation on the SLIM normal force characteristics. For one-layer thickness (.0185 inches), the normal force at 20 Hz/sec is approximately one-third the force developed with 1/16 inch thick iron backing.

A point of interest, and worth noting, is the fact that the magnitude of SLIM normal force at the frequency corresponding to peak thrust (40 Hz/sec in Figure 22), is about one-half its value in the limit of low stator excitation frequencies. This functional dependence observed with iron backing is analogous to that observed for metal-only secondaries in which normal force at the frequency of peak thrust was approximately one-half its value in the limit of high stator excitation frequencies.

2.4.4 Composite SLIM Reaction Forces-versus-Laminated and Non-laminated Iron Backing

Studies were next made to examine the effect of laminating the back iron on the reaction force characteristics. The back iron layer was formed from 1/4 inch wide insulated strips of M-19, Gage 26, steel, stacked to a height of 6 inches. The laminated back iron was positioned on the back surface of the 10" x 1/8" aluminum secondary plate as shown in Figure 16.

Data of SLIM thrust-versus-stator excitation frequency is given in Figure 24 for the laminated and nonlaminated SLIM configurations. Tests were conducted with stator currents held constant at 10 and 14 amperes. The nonlaminated iron specimen comprised a 1/4 inch thick Type 1018 steel plate. The laminated steel produced about a ten percent increase in SLIM thrust compared with the plate steel.

Curves of SLIM thrust, computed on the basis of the finite-secondary-thickness iron backing model presented in Section 2.3.4, are given in Figure 24. The curves were computed for iron conductivities of 0, 10^7 mhos/m corresponding to laminated and nonlaminated iron backing respectively. Airgap distance was taken as 1.5 mm. The correlation of the computed and measured thrust was quite good above the excitation frequency of 100 hertz/second but deviated considerably below it. (The data taken at a stator current of 14 amps was limited to frequencies below 135 Hz/sec due to the power lamitation of the source supply. The computed thrust had a peak value about fifty percent greater than the measured peak thrust and occurred at a frequency below that of the measured peak thrust. These results are in substantial agreement with those previously presented in Figure 22. The SLIM with the laminated iron backing developed a thrust about ten percent greater than with the nonlaminated iron backing. The computed curves showed a similar difference between the corresponding sets of curves, though somewhat smaller in magnitude.

The skin depth in iron is independent of frequency for zero conductivity (laminated) iron and is inversely proportional to the propagation number. For the SLIM being studied, the skin depth in laminated iron is .0182 meters or about three times the thickness of the laminated iron backing specimens. The skin depth in the solid (nonlaminated) iron plate is considerably less than in the laminated steel, except near zero frequency. At 20 Hz/sec, the skin depth is .0011 m or about one-sixth the iron plate thickness and at 200 Hz/sec, the skin depth is .00035 m or about one-twentieth the plate thickness. The large difference in skin depths between laminated and solid iron backing appeared to have little effect on the thrust developed by the SLIM for the range of stator excitation frequencies investigated. The ten percent increase in measured thrust for the laminated iron backing might be due to the superior electrical properties of the M-19 steel compared with that of the Type 1018 steel. Electrical M-19 steel possesses a higher permeability and a lower core loss than does Type 1018 steel.

The corresponding data of normal force as a function of stator excitation frequency is given in Figure 25 for the laminated and nonlaminated iron backing secondaries. As in the case of the thrust data, a somewhat larger normal force was observed over the range of frequencies measured for the laminated iron compared with the plate iron structure. The conclusion arrived at for the thrust data applies equally to the normal force data. The form of the force-

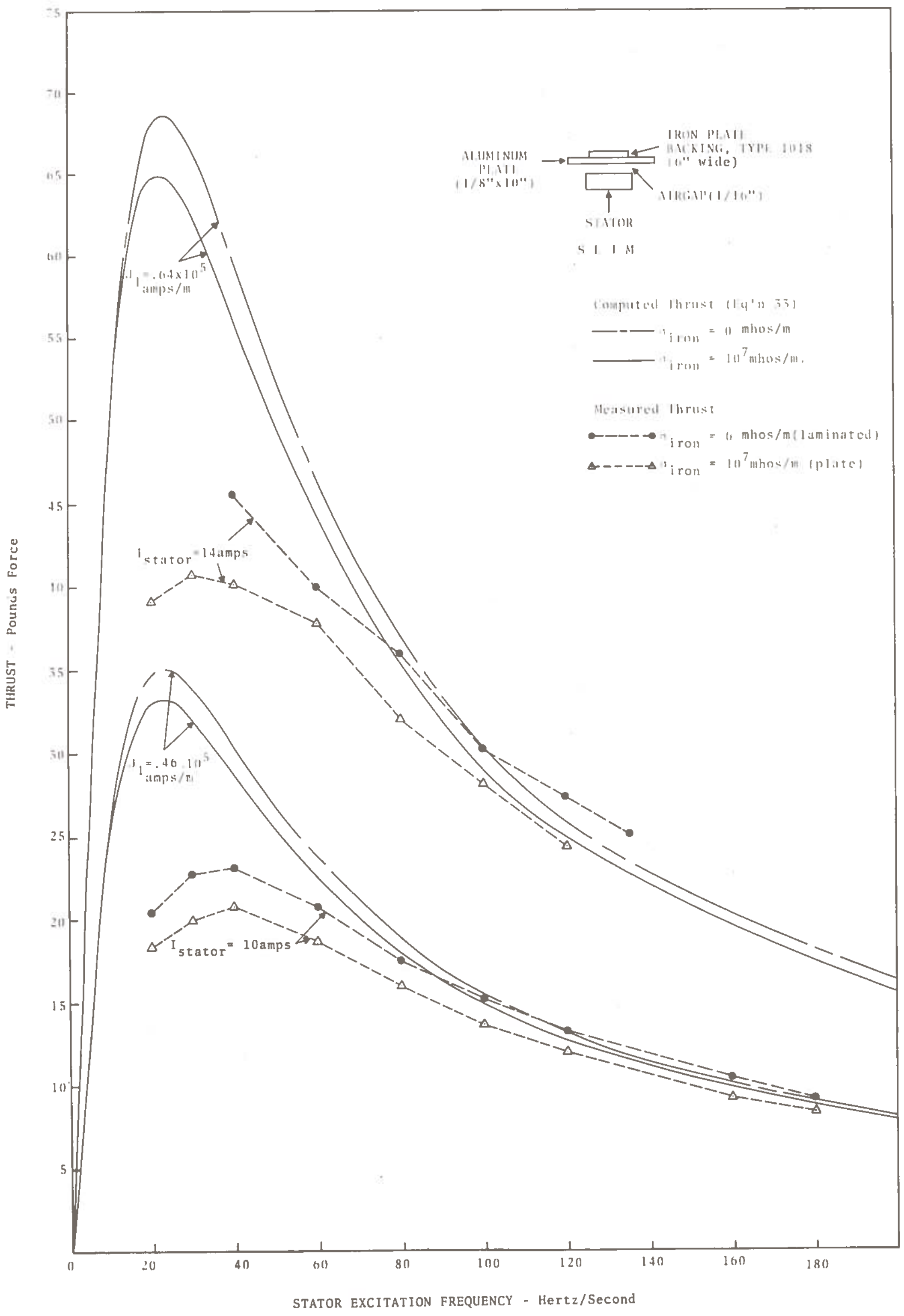

Figure 24. Measured SLIM Thrust-versus-Stator Excitation Frequency for Laminated and Nonlaminated Iron Backing Secondaries

versus frequency characteristics is in good agreement with the previous SLIM data presented in Figure 23.

Curves of computed normal force based on the SLIM model described in Section 2.3.4 are also shown plotted in Figure 25. The deviation between theoretical curves for the laminated (zero conductivity) and nonlaminated (nonzero conductivity) SLIM secondaries is about the same order of magnitude as that observed in the measured data. The relatively small difference in the forces developed by the laminated and non-laminated SLIM secondaries agrees with the conclusions reached in the Section 2.3.4.

The use of laminated-versus-nonlaminated steel in a composite SLIM secondary poses a number of interesting questions. With nonlaminated steel, the eddy currents tend to repel the flux from the iron region and produce high peak flux densities at the incident interface. The confinement of the incident flux to a skin depth thickness in the iron promotes magnetic saturation in the surface region of the iron. With magnetic saturation, the permeability of the saturated iron will be reduced to a value consistent with the flux density characteristics of the iron and the wave solution of the composite secondary structure. Since the flux density attenuates exponentially with penetration depth inside the iron, (in the absence of saturation), it is likely that the iron permeability (under conditions of surface magnetic saturation) will increase rapidly with penetration depth and thus maintain the rather abrupt impedance discontinuity characteristic of the metal-iron interface. There remains a number of unanswered questions dealing with the electromagnetic characteristics of composite SLIM secondaries and further experimental work in this direction would be most helpful.

2.4.5 <u>Lateral Force-versus-Displacement of Secondary from Mid-Symmetry Position</u>

The SLIM lateral force in the z-direction is examined in this section to determine its magnitude and dependence on the relative displacement of the secondary from the midplane of the stator. To

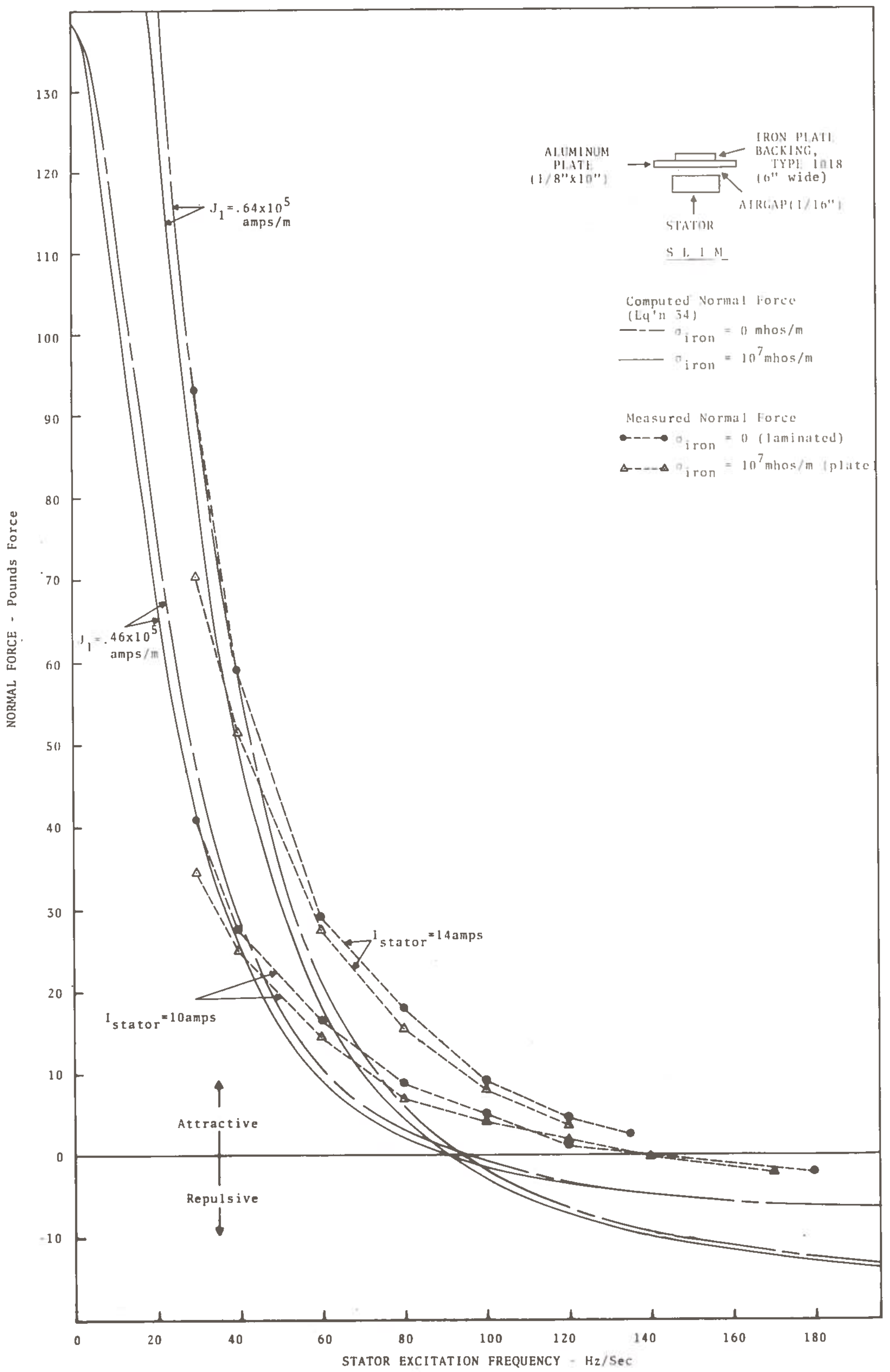

Figure 25. Measured SLIM Normal Forces versus Stator Excitation Frequency for Laminated and Nonlaminated Iron Backing Secondaries

facilitate the measurement of lateral forces, the test setup was altered to provide freedom for the stator to move in the z-direction, instead of the x-direction as in the previous reaction force studies. A 200 pound transducer was positioned at one side of the stator to measure the lateral force. To eliminate the effect of the frictional force on the lateral force measurements, a tension force of constant amplitude was applied to the stator side opposite to the force transducer. The secondary test structures were rigidly fixed in position as in all previous tests. Measurements of the lateral force were then made as the secondary 'rail' was displaced relative to the center axis of the SLIM.

The initial test undertaken with aluminum-only secondaries gave almost no measurable lateral force as a function of secondary displacement with the stator operated at rated current levels (18 amperes). The magnitude of the observed lateral force was estimated to be only several percent of the thrust force, and were not much greater than the minimum force capable of being resolved.

The lateral force developed with an iron plate secondary was next investigated. An iron plate 6 inches wide and 1/2 inch thick was positioned a distance of 3/16 inch above the surface of the stator. The stator current was maintained constant at 14 amperes and the excitation frequency held fixed at 40 Hz/sec. The measured lateral force as a function of displacement distance from the stator midplane is shown in Figure 26. The lateral force increased linearly with initial displacement, remained constant over a displacement distance somewhat less than the width of the secondary plate, and finally increased followed by a rapid decrease to zero. At the displacement distance of 6 inches, corresponding to a plate overlap of one inch with the stator surface, the lateral force was maximum. At the displacement distance of 7 inches, corresponding to zero overlap, the lateral force was null. It is apparent from a study of the test data, that the lateral <u>force density</u> is maximum at the stator edges and decreases rapidly to zero for displacement distances on either side of the stator edge.

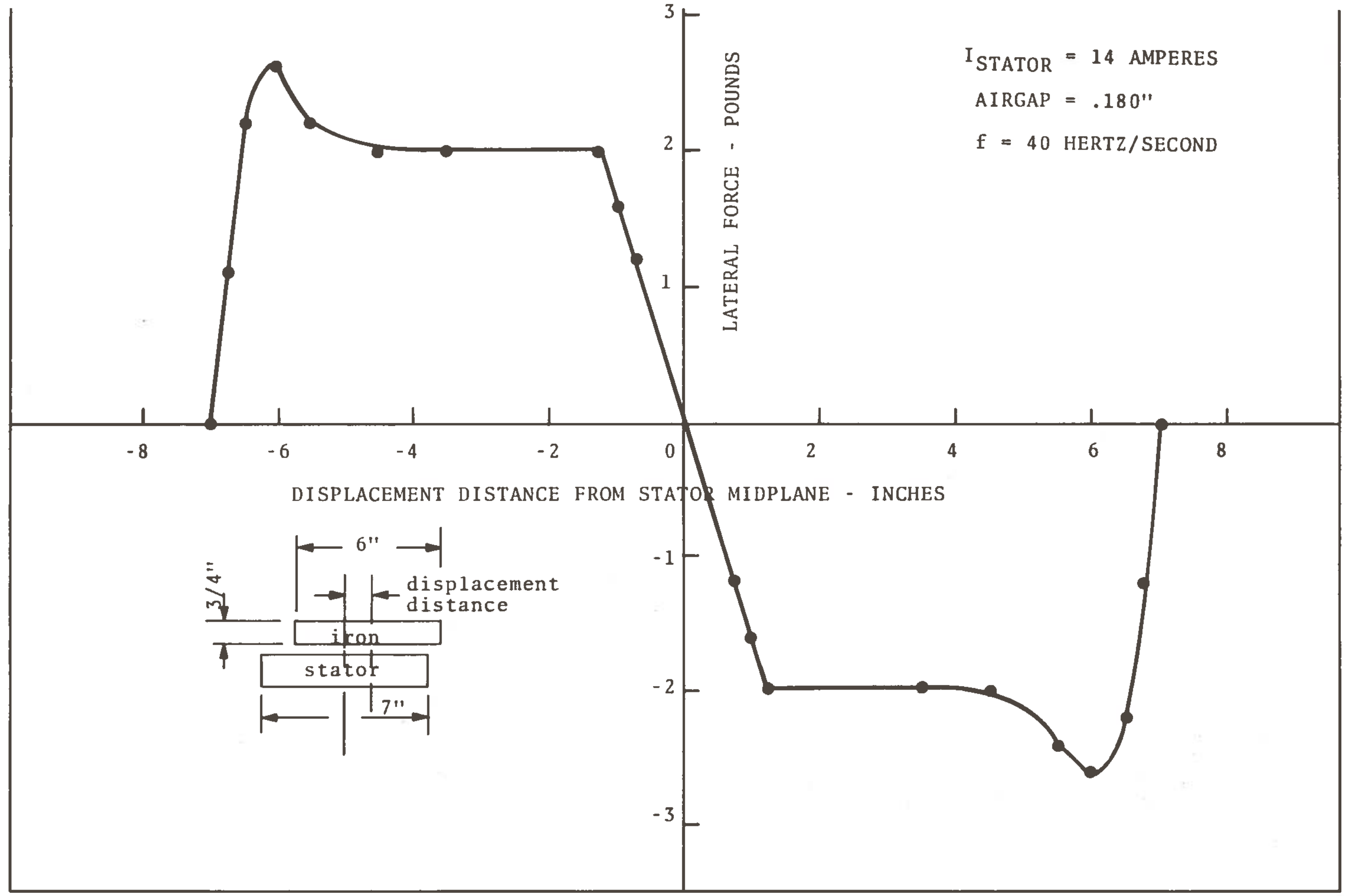

Figure 26. SLIM Lateral Force as a Function of Displacement Distance of Secondary Plate from Stator Midplane Position

3. CONCLUSIONS

This report summarized the reaction force data measured on a laboratory SLIM and the correlation of this data with theory based on idealized SLIM models. The first part of the report discussed the limiting forms of the solutions derived for single- and multi-region SLIM secondaries using models which replace the stator by an equivalent current density wave. Theoretical expressions were derived for SLIM thrust and normal forces under prescribed conditions. The effect of SLIM geometry and related boundary conditions on the reaction forces was inferred from the study of the computed and measured reaction force data.

The conclusions of this report are divided into two parts, the first part dealing with theoretical matters discussed in this report, and the second part with the results of experiments on particular SLIM configurations. The conclusions are listed separately by number. These are followed by recommendations for future SLIM study programs.

1. The study of SLIM models involving single-region secondaries shows that SLIM thrust peaks at a given slip frequency determined by the dimensional and electromagnetic parameters characterizing the SLIM, while the normal force increases monotonically with slip frequency. For the case of the infinite thickness secondary with vanishingly small airgap, the normal force attains one-half its limiting magnitude at high frequencies with the slip frequency adjusted for maximum thrust. The maximum thrust decreases in magnitude with increase in airgap and shifts in the direction of higher frequencies.

2. The infinite thickness SLIM model and the finite thickness model give comparable results as long as the thickness of the SLIM secondary is substantially <u>greater</u> than the skin depth. For secondary thickness less than or the same order of magnitude as the skin depth, the finite thickness metal must be used for more

accurate results. The latter predicts a shift in peak thrust towards higher frequencies for secondary thicknesses less than the skin depth. This shift in frequency, which is attributed to an increase in the effective secondary resistance when the secondary thickness is less than the skin depth, has been confirmed by reaction force studies conducted in the laboratory.

3. The thin-sheet approximation model and the finite thickness model give comparable results as long as the thickness of the SLIM secondary is substantially <u>less</u> than the skin depth. The thin-sheet model predicts the frequency of peak thrust to vary inversely with secondary thickness, and linearly with airgap separation for small airgap separation distances.

4. The analysis of the SLIM model for a composite metal-ferromagnetic secondary indicates SLIM thrust can be substantially increased by the addition of ferromagnetic (iron) backing, while the <u>repulsive</u> normal forces are reduced by the addition of ferromagnetic backing. At low 'slip frequencies', the normal forces are generally attractive, due to the dominant attractive force associated with the magnetic back iron. The transition from attractive to repulsive normal forces occurs at a frequency determined by the magnetic Reynolds number characterizing the SLIM secondary. The analysis predicts a shift in the peak thrust towards lower frequencies with increasing ferromagnetic backing thickness, for backing thickness less than 0.5 millimeters. For a larger backing thickness, thrust is expected to be relatively independent of backing thickness. The thin-sheet approximation applied to the composite SLIM gave theoretical reaction forces which agreed reasonably well with the forces computed using the exact-finite thickness model, for excitation frequencies above 30 Hz/sec and ferromagnetic backing thickness greater than 0.5 mm.

5. The calculation of thrust and normal forces for laminated-versus-nonlaminated (i.e., zero-versus-nonzero electrical conductivity) backing suggests that only a relatively small increase in SLIM forces results from the use of laminated instead of nonlaminated ferromagnetic backing.

6. The computer calculations for six examples of magnetic flux diffusion in composite SLIM secondaries show the effect of backing thickness and conductivity on flux penetration along the normal y-direction. The flux density plots indicate that non-laminated ferromagnetic backing produces higher flux densities in the ferromagnetic region near the (metal-ferromagnetic) interface than would occur using laminated ferromagnetic backing. This could produce localized regions of magnetic saturation in a limited depth inside the ferromagnetic region and alter the magnetic permeability along both the normal (y) and thrust (x) directions.

The correlation between measured and computed reaction forces was generally fair to good, except for the thrust studies on the composite SLIM, which gave poor results at lower excitation frequencies. Part of the discrepancies between theory and experiment could be due to higher-order spatial harmonics in the airgap flux distribution. It is likely that some improvement in correlation could be achieved if the forces were computed directly from the measured flux distribution in the airgap of the SLIM.

a. The minimum thickness of back iron required for effective operation of the LIM TECH stator is about 1/16 inch for a stator current of 10 amps. Larger back iron thickness produced no substantial increase in either the thrust of the normal force. Smaller back iron thickness resulted in magnetic saturation over the range of stator excitation frequencies tested.

b. The SLIM thrust and normal forces developed with a back iron width equal to that of the stator was about 85 percent of the maximum force realizable with the back iron extended to a 'large' distance beyond the stator width.

c. The use of laminated iron in place of solid iron plate in a composite aluminum-iron secondary gave approximately a ten percent increase in thrust and normal force. Evidence indicates that part of this increased force contribution is due to the superior electrical properties of the laminated steel.

d. The lateral reaction forces (z-direction) were observed to be almost two orders of magnitude smaller than the measured thrust and normal forces.

A review of the work described in this report reveals a number of fruitful areas for future analytical and empirical SLIM studies. Little has been published in the literature on the wave solutions of SLIM models other than mathematical treatments of the simplified infinite SLIM model. Studies of boundary related effect, i.e., edge-effects, end-effects, which have been undertaken for the double-sided LIM, have yet to be considered for the SLIM. The effect of secondary back iron saturation on SLIM performance is another area awaiting treatment. Such studies would be helpful in refining the SLIM model and improving its effectiveness to describe in practical SLIM.

Additional laboratory studies would also be desirable. Mapping the flux distribution over the stator surface would be helpful in relating the SLIM stress density to the winding configuration and geometry. The measured airgap flux distribution in a SLIM with secondary iron backing could be compared with the related flux distribution predicted by Bolton for the double-sided LIM. An important consideration for a practical SLIM is the lateral (side) forces developed when the secondary is positioned asymmetrically with respect to the primary. Since the SLIM stress components over the stator surface are intimately related to the surface flux density distribution, these studies could complement one another. The shaping flux distribution by shading pole techniques is likely to be another area offering possibilities for development. These are a few of many possible areas suggested for future investigations.

REFERENCES

1. Ooi, B.T. and White, D.C. "Traction and Normal Forces in the Linear Induction Motor," Trans. IEEE, PAS-89, No. 4, 1970, pp. 838-45.
2. Lipkis, R.S. and Wang, T.C. "Single-Sided Linear Induction Motor (SLIM): A Study of Thrust and Lateral Forces," for Dept. of Transportation, DOT Report No. FRA-RT-72-25, PB#205 029, June 1971.
3. Cullen, A.L. and Barton, T.H. "A Simplified Electromagnetic Theory of the Induction Motor, Using the Concept of Wave Impedance," Proc. IEEE, Vol. 1050, (8), pp. 331-36, 1958.
4. Russell, R.L. and Norsworthy, K.H. "Eddy Current and Wall Losses in Screened-Rotor Induction Motors," Proc. IEEE, Vol. 105A, pp. 163-75, 1958.
5. Bolten, H., "Transverse Edge Effect in Sheet-Rotor Induction Motors," Proc. IEEE, Vol. 116, (5), pp. 725-31, 1969.
6. Bolten, H., "Forces in Induction Motors with Laterally Asymmetric Sheet Secondaries," Proc. IEEE, Vol. 117, pp. 2241-49 1970.
7. Dukowicz, J.K. "The Single-Sided LIM with Saturated Back Iron," for Dept. of Transportation, Report PB#207 327.
8. Yee, H. and Wilson, T. "Saturation and Finite-Length Effects in Solid-Rotor Induction Machines," Proc. IEEE, Vol. 119, No. 7, pp. 877-82, 1972.
9. Woodson, H.H. and Melcher, J.R., Electromechanical Dynamics, Part II, John Wiley & Sons, New York, N.Y. 1968.
10. Theory of Linear Induction Motors, Yamamura, S., John Wiley & Sons, New York, N.Y. 1972, p. 15.
11. "Study of Linear Induction Motor and Its Feasibility for High-Speed Ground Transportation," for Department of Transportation Report No. PB#174 866, June 1967.

12. Laithwaite, E.R., "Some Aspects of Electrical Machines with Open Magnetic Circuits", Proc. IEEE, Vol. 115, No. 9, pp. 1275 - 1282.

13. Greig, J., and Freeman, E.M. "Traveling Wave Problem in Electrical Machines," Proc. IEEE, Vol. 114, No. 11, pp. 1681 - 83, 1967.

14. Fitzgerald, A.F., and Kingsley, C., Electric Machinery, McGraw-Hill, New York, N.Y. 1961.